



Title	Analysis of the mechanism in gut morphological formation : Spatiotemporal control during mouse duodenojejunal flexure formation
Author(s)	尾之内, 佐和
Citation	北海道大学. 博士(獣医学) 甲第12362号
Issue Date	2016-06-30
DOI	10.14943/doctoral.k12362
Doc URL	http://hdl.handle.net/2115/62605
Type	theses (doctoral)
File Information	Sawa_Onouchi.pdf



[Instructions for use](#)

**Analysis of the mechanism
in gut morphological formation
- Spatiotemporal control during mouse
duodenojejunal flexure formation -**

腸管の形態形成機序の解析

—マウス十二指腸空腸曲形成にみられる時空間的制御—

Sawa Onouchi

Laboratory of Anatomy

Department of Biomedical Sciences

Graduate School of Veterinary Medicine

Hokkaido University

Abbreviations

AJ: adherens junction

α SMA: alpha-smooth muscle actin

B6: C57BL/6

BMP: bone morphogenetic protein

BrdU: Bromodeoxyuridine

CB: cacodylate buffer

Cdx2: caudal type homeobox 2

CD31: CD31 antigen

CD34: CD34 antigen

CE: convergent extension

DAB: 3,3'-diaminobenzidine tetrahydrochloride

DJF: duodenojejunal flexure

E: embryonic day

E-cadherin: cadherin 1

ECM: extracellular matrix

FGF: fibroblast growth factor

HE: hematoxylin-eosin

IntDen: integrated density

LYVE-1: lymphatic vessel endothelial hyaluronan receptor 1

MMP: matrix metalloproteinase

P: postnatal day

PB: phosphate buffer

PBS: phosphate-buffered saline

PCP: planar cell polarity

PFA: paraformaldehyde

RT: room temperature

SE: standard error

Sox10: SRY [sex determining region Y]-box 10

TEM: transmission electron microscope

TGF β : transforming growth factor- β

Tuj1: tubulin, beta 3 class III

Indexes

Preface	1
Chapter 1 Gut morphology and running pattern in postnatal and prenatal mice	4
Introduction	5
Materials and Methods	6
Results	8
Discussion	11
Summary	14
Tables and Figures	16
Chapter 2 Histological features of the mouse fetal duodenojejunal flexure	21
Introduction	22
Materials and Methods	24
Results	30
Discussion	34
Summary	39
Tables and Figures	41
Chapter 3 Asymmetric distribution of the gut component cells and molecules observed in the developing mouse duodenojejunal flexure	53
Introduction	54
Materials and Methods	56
Results	63
Discussion	72

Summary	82
Tables and Figures	83
Conclusion	100
References	105
Acknowledgements	112
Conclusion in Japanese	113

Preface

The gut morphology effects on the digestive function and is related to feeding habit of each species. For example, the morphology of the ascending colon is different among species: double-folded U-shape in horses, conical spiral in pigs, and disklike spiral in ruminants. These morphological differences might be related with the digestive function of each species. In addition, bowel obstruction due to malrotation and atresia are reported in around 6 per 10,000 live human infants (Adams and Stanton, 2014). Intestinal malrotation is a deformity with an abnormality in intestinal positioning and may develop to intestinal volvulus and acute emergency. Intestinal malrotation presents in around 1 in 2,500 live human infants. However, its incidence including the case without symptoms is much higher than this, suggested as 0.2%–1% of the normal population (Adams and Stanton, 2014). That population with latent malrotation also has a potential for developing intestinal volvulus in their lifetime (Nehra and Goldstein, 2011). Therefore, elucidating gut morphogenesis gives important information for understanding gut physiology and pathology.

The process of gut morphogenesis in mammals has been well studied in mice. After gastrulation, gut morphogenesis in mice starts as pits which will give rise to the cranial intestinal portal and the caudal intestinal portal, at around embryonic day (E) 7.0. At E8.0, the cranial and caudal intestinal portals are clearly visible. Between E8.0 and E9.0, the lips of both portals move toward each other and the lateral endoderm folds ventrally. Between E9.0 and E9.5, the endoderm surrounded by mesenchyme finishes folding and

exists as a closed gut tube which consists of foregut, midgut, and hindgut. Simultaneously, the midgut begins to make a primary loop and grows into the umbilical cord as physiological umbilical herniation at around E10.5. This herniation continues until around E16.0. During primary gut loop formation to physiological herniation, the gut tube experiences rotation, elongation, and flexure formation (Noah et al., 2011; Spence et al., 2011). Flexure formation is an important process for compaction of the long gut tube to fit into the abdominal cavity. A recent study in chicks and mice reported that gut looping in the jejunum occurs due to difference in elongation rates of the gut tube and its dorsal mesentery (Savin et al., 2011).

Thus, the morphological mechanisms of gut morphogenesis are being revealed gradually. However, the mechanisms of gut morphogenesis, in particular flexure formation, have not been investigated enough. In this study, the author focused on the developmental process of the mouse duodenojejunal flexure (DJF) as a model for flexure formation and investigated the morphogenetic mechanisms of flexure formation.

Further, the author revealed several asymmetric morphologies between the inner and outer bending sides of the mouse DJF. From these findings, the author hypothesized that the gut tube, at least the DJF, can make a flexure by the gut original power. This hypothesis is novel approach for elucidating gut flexure formation. Interestingly, some recent researchers suggest that duodenum looping including the DJF contributes to gut rotation (Kluth et al., 2003). Moreover, the mechanism under the morphogenesis of the species-specific ascending colon remain a mystery in the veterinary field, but the morphological

change in the developing ascending colons of equine, bovine, and swine embryos which have the unique morphologies seemed to be similar with that of the DJF (Noden and Laphunta, 1991). Therefore, this study would give good understandings for gut formation in mammalian embryology. This thesis contains three chapters; the first chapter explores the suitable part of the gut tube to investigate flexure formation by observing the gut morphology in postnatal and prenatal mice, and the second chapter examines the histological features in the developing mouse DJF as a model for flexure formation. Finally, the third chapter examines the distribution of the gut component cells and extracellular matrix molecules in the developing mouse DJF, as important factors for establishing the morphological features observed in the second chapter.

Contents of this research were published in the following articles.

1. Onouchi, S., Ichii, O., Otsuka, S., Hashimoto, Y., Kon, Y. 2013. Analysis of duodenojejunal flexure formation in mice: implications for understanding the genetic basis for gastrointestinal morphology in mammals. *J. Anat.*, **223**: 385-398.
2. Onouchi, S., Ichii, O., Otsuka-Kanazawa, S., Kon, Y. 2015. Asymmetric morphology of the cells comprising the inner and outer bending sides of the murine duodenojejunal flexure. *Cell Tissue Res.*, **360**: 273-285.
3. Onouchi, S., Ichii, O., Nakamura, T., Elewa, Y. H., Kon, Y. Spatiotemporal distribution of extracellular matrix changes during mouse duodenojejunal flexure formation. *Cell Tissue Res.*, in press.

Chapter 1

Gut morphology and running pattern

in postnatal and prenatal mice

Introduction

Recently, several morphological mechanisms about gut development have been proposed. The mechanism of gut morphogenesis, in particular gut flexure formation, is also being uncovered. It has been reported that the different elongation rate between the gut tube and its dorsal mesentery contributes to flexure formation in the jejunum and ileum (Savin et al., 2011). Interestingly, there are the species-specific differences in the gut morphology; the ascending colon is folded in horses, spirals conically in pigs, and disklike in ruminants. Those ascending colons contain one central flexure which elongates and spirals. This morphological feature is quite different from the flexures in the jejunum and ileum. Therefore, the author hypothesized that there are several mechanisms of gut flexure formation.

As a mechanism to make a morphological feature of the gut tube, the contributions of the mesentery and body axes formation are proposed. The left-right differences in the morphology and gene expressions of the dorsal mesentery were reported to contribute gut morphogenesis such as the gut tube rotation and looping in the future jejunum (Davis et al., 2008; Kurpios et al., 2008; Plageman et al., 2011).

In this chapter, the author investigated the mouse gut morphology and found unique morphological changes in DJF formation different from those in the herniation of the jejunum. Therefore, the author investigated mouse DJF formation in the following research as a flexure formation model to elucidate a novel mechanism in gut flexure formation.

Materials and Methods

Ethical Statement

This study was approved by the Institutional Animal Care and Use Committee convened at the Graduate School of Veterinary Medicine, Hokkaido University (approval no. 13-0032). The investigators adhered to *The Guide for the Care and Use of Laboratory Animals of Hokkaido University, Graduate School of Veterinary Medicine* (approved by the Association for Assessment and Accreditation of Laboratory Animal Care International).

Animals and Sample Preparations

C57BL/6 (B6) mice with age of postnatal day (P) 0–50 were maintained in our specific pathogen free facility and used in this study. In addition, B6 pregnant mice carrying embryos with age of E10.75–13.75 were purchased from Japan SLC, Inc. (Shizuoka, Japan). Noon on the day when a vaginal plug was found was considered as E0.5. These mice were subjected to deep anesthesia by pentobarbital sodium 60 mg/kg administered intraperitoneally and euthanized by exsanguination from the carotid arteries. Subsequently, the postnatal and prenatal gut tubes were collected and fixed with 10% neutral buffered formalin and 4% paraformaldehyde (PFA) in 0.1M phosphate buffer (PB; pH 7.4) at 4°C overnight, respectively. The gut morphology and running pattern were observed. As for embryonic gut tubes, the attaching position of the dorsal mesentery was also observed by a dissection microscope (SZX7, Olympus, Tokyo, Japan). A part of the gut tubes were separated

from the body and used for detailed observation.

Histological Analysis

In order to observe the attaching portion of the dorsal mesentery, the fixed fetal gut tubes were embedded in paraffin. The cross- and sagittal-semi-serial sections (3–4- μm -thick) of the DJF at E10.75–13.75 were used for hematoxylin-eosin (HE) staining.

Results

Gut Morphology and Running Pattern in Postnatal Mice

To investigate the gut flexure pattern, the morphologies and running patterns of the gut tubes were observed in the postnatal and prenatal mice (Figs. 1-1 and 1-2). In the postnatal mice (Figs. 1-1a–l), although the intestines differently ran at the same age (Figs. 1-1a–h), the common running patterns and flexures were partially observed such as the descending and ascending parts of the duodenum, those of colon, the cranial and caudal flexure of the duodenum, and the DJF (Figs. 1-1b, d, f, h, j and l). On the other hand, the jejunum and ileum did not have exactly same flexures (Figs. 1-1c, g and k), and the portions of the cecum was different among the postnatal mice (Figs. 1-1d, h and l).

Gut Morphology and Running Pattern in Prenatal Mice

In the prenatal mice, every gut tube ran on the same pattern among fetal mice at the same embryonic days (Fig. 1-2). At E10.75, the gut tube was a straight tube with a slight flexure of the primary loop in the midgut (Fig. 1-2a). At E11.25–E11.75, the primary loop appeared as an obvious flexure and elongated toward the ventral side and out of the body as physiological umbilical herniation, and the gut tube started to rotate clockwise around the cranial mesenteric artery (Fig. 1-2b). At E12.75 and E13.75, the primary loop formed complex flexures out of the body (Figs. 1-2c and d).

In particular, the DJF was clearly observed as independent flexure through the period from E10.75 to E13.75 (Figs. 1-2a–d). Therefore, the author selected the mouse DJF

among the examined gut flexures as a useful model to analyze flexure formation. The DJF was located in the abdominal cavity, not out of the body, during the examined period. The flexure appeared at the region located at the caudal position of the pancreatic buds (Figs. 1-2a and b). The DJF formations were classified into 3 stages according to their existence and position of the flexure; i) the expansion stage characterized by the increased gut diameter without clear flexure (Fig. 1-2a), ii) the flexure formation stage characterized by the flexure along the dorsal-ventral body axis (Fig. 1-2b), and iii) the flexure elongation stage characterized by the elongated flexure around the stomach with elongating legs passing from caudal to left of the stomach to turn its tip toward the cranial direction (Figs. 1-2c and d).

Attaching Portion of the Dorsal Mesentery in the Developing Mouse DJF

In order to assess the contribution of the dorsal mesentery to DJF formation, the attaching portion of the dorsal mesentery in the fetal gut tube was analyzed in the each DJF stage (Fig. 1-3). At the expansion stage, the dorsal mesentery attached to the nearly dorsal side of the gut based on the body axis (Fig. 1-3a). The cross-section of the fetus at the expansion stage also revealed that the gut tube was hanged by dorsal and ventral mesenteries with a tilt toward the left side of the body axis (Fig. 1-3b). At the flexure formation stage, based on the body axis, the right side of the DJF was uncovered with the mesentery, while the left side of the DJF was covered (Figs. 1-3c and d). In the sagittal-section, the dorsal mesentery did not appear on the outline of the DJF (Fig. 1-3e). This result meant that the dorsal mesentery attached to the left side of the DJF based on the

body axis, in other words, the DJF was formed along the left-right intestinal axis. At the flexure elongation stage, the dorsal mesentery was attached across the two gut tube legs forming the ascending and descending portions of the DJF (Figs. 1-3f and g). The attaching position of the dorsal mesentery was a lateral side of the DJF facing the stomach (Fig. 1-3h). These results meant that the attaching direction of the dorsal mesentery to the DJF (the left-right body axis) did not correspond with the bending direction of the DJF (the dorsal-ventral body axis) during DJF formation (Fig. 1-3i), since the DJF rotated counterclockwise in about 90° around the cranial-caudal intestinal axis.

Discussion

The postnatal mice had the both common and uncommon flexures in the guts among individuals. The common flexures contained the cranial and caudal flexure of the duodenum, the DJF, and the colic flexures (Dyce et al., 1998; König and Liebich, 2007). On the other hand, the uncommon flexures were observed in the jejunum and ileum. Interestingly, the morphological features seemed to be different between the common and uncommon flexures; the former was quite simple to be easily differentiated from each individual flexure; the latter sometimes overlapped each other. In postnatal age, eating and digesting cause the peristalsis to change the position of the gut in the abdominal cavity. During the peristalsis, the gut contract and stretch to form the irregular flexures covering the regular flexures conserved among individuals (Dyce et al., 1998). Furthermore, some parts of the gut, especially the jejunum, and ileum are less tightly fixed with the mesentery to the abdominal wall (Dyce et al., 1998; König and Liebich, 2007). Therefore, the environmental factors participate in the formation of the gut morphology, in particular at the jejunum and ileum, in the postnatal mice, while the duodenum and colon are less affected by the environmental factors.

In the prenatal mice, every gut tube ran on the same pattern among individuals during the examined embryonic days (E10.75–E13.75). In the earlier prenatal life, the gut tube is still under the developmental processes such as morphological changes and cell differentiation in the mucosa or mesenchyme (Noah et al., 2011; Powell et al., 2011). Therefore, it was considered that the gut morphology was not

affected by the peristalsis derived from the contraction of the smooth muscles. Interestingly, the author could observe two locations where flexure formation occurred: the herniation and the DJF. At the herniation, there were complex flexures which were difficult to identify each flexure. On the other hand, the DJF was independently and clearly observed apart from the herniation in the jejunum. From these results, the author considered that there are at least two types of the mechanism of flexure formation. Since the mouse DJF was observed throughout prenatal and postnatal gut tubes, the DJF was the most useful site for elucidating gut flexure formation.

Recently, the dorsal mesentery was reported to contribute the chick and mouse gut morphology such as gut rotation and looping in the future jejunum (Davis et al., 2008; Kurpios et al., 2008; Savin et al., 2011). In this study, the dorsal mesentery attached to the nearly dorsal side of the mouse DJF based on the body axis at the expansion stage. However, according to the author's investigation, at the flexure formation stage, the dorsal mesentery attached to the left lateral side of the DJF based on the body axis. Furthermore, at the flexure elongation stage, the dorsal mesentery attached to the one lateral side of the DJF facing to the stomach. These observations suggested that the dorsal mesentery was located on the left lateral side, not on the dorsal side, of the DJF based on the body axis during mouse DJF formation. Importantly, the DJF bended toward dorsal direction along the body axis at the flexure formation stage. Therefore, the author proposed that the dorsal mesentery does not contribute to mouse DJF formation via the same mechanism of

flexure formation in the jejunum because the direction of its attachment (left side of the body axis) does not correspond with the bending direction of the DJF (dorsal side of the body axis). This result suggests that mouse DJF formation contains another mechanism of flexure formation beyond that in the jejunum.

In the following study, the author focused on mouse DJF formation because the mechanism under DJF formation might be a novel one different from that revealed in other reports.

Summary

The gut morphology affects the digestive system and is characterized by species-specific feeding habits. In addition, its congenital deformities including malrotation are reported in both human and animal. Therefore, to elucidate gut morphogenesis gives good understandings for gut physiology and pathology. The author focused on gut flexure formation due to its importance for the gut morphological features. Recent studies have reported that flexure formation in the jejunum and ileum is achieved by the interaction between the gut tube and dorsal mesentery. However, flexure formation in other parts is still unknown. Therefore, the author investigated gut flexures in the developing mouse gut tube to elucidate another mechanism for flexure formation.

The postnatal gut tube contains two types of the flexure morphology. The one is easily differentiated from each individual flexure. The other is too complex to divide flexures into an individual one because they overlap each other. The former type is observed in the duodenum including the DJF, and the colon, and the latter type is observed in the jejunum and ileum. The difference between both types seems to be the effect of peristalsis. The duodenum and colon are tightly attached with the abdominal cavity via the dorsal mesentery, while the jejunum and ileum are loosely attached. Therefore, the peristalsis affects the gut morphology and changes its shape more easily at the latter than at the former. On the other hand, the prenatal gut tube had a common shape at the same age. Interestingly, the author could also observe two types of the flexure morphology. At the herniation of the jejunum, it was

difficult to identify each flexure due to its complex appearance, while the DJF was a simple flexure. In addition, the dorsal mesentery of the DJF was changed its position along the body axis from the dorsal to the left side of the gut tube, while DJF formation occurred along the dorsal-ventral body axis. This suggests that the dorsal mesentery of the DJF does not affect DJF formation via the same way of flexure formation in the herniation.

These findings suggest that there are two types of the flexure morphology and that the mechanism of mouse DJF formation is different from that of flexure formation in the jejunum related to the cooperation with the dorsal mesentery. In this chapter, the author revealed the mouse DJF as a flexure formation model for elucidating a novel flexure formation mechanism.

Tables and Figures

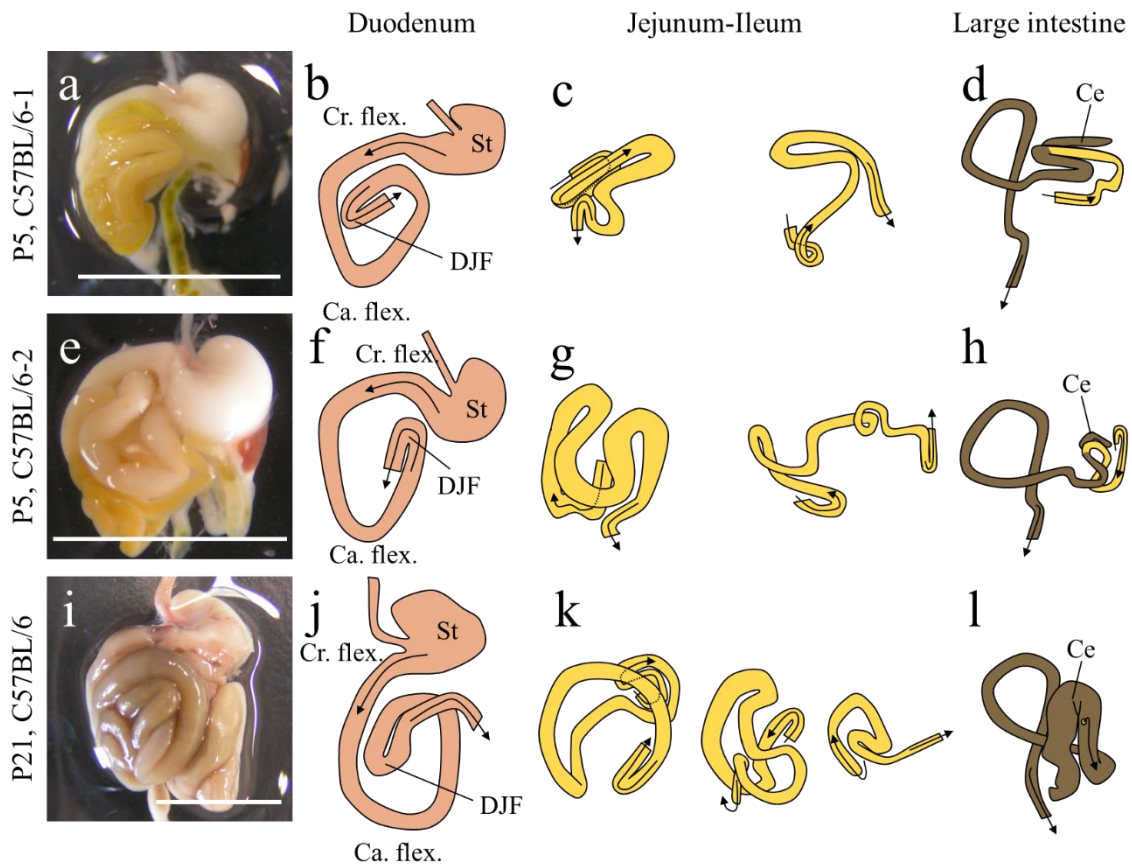


Figure 1-1. Gut morphology in postnatal mice.

(a and e) Whole-gut tube of the P5 mouse, individual number 1 (a) and 2 (e).

(b-d) and (f-h) Sketches of (a) and (e) divided into three parts: stomach (St) and duodenum (b and f), jejunum and ileum (c and g), large intestine including cecum, colon and rectum (d and h).

(i) Whole-gut tube of the P21 mouse.

(j-l) Sketches of (i) divided into three parts: St and duodenum (j), jejunum and ileum (k), large intestine including cecum, colon and rectum (l).

Arrows, running direction of the gut tube; bars, 1 cm; Ca. flex., caudal flexure of the duodenum; Ce, cecum; Cr. flex., cranial flexure of the duodenum; DJF, duodenojejunal flexure.

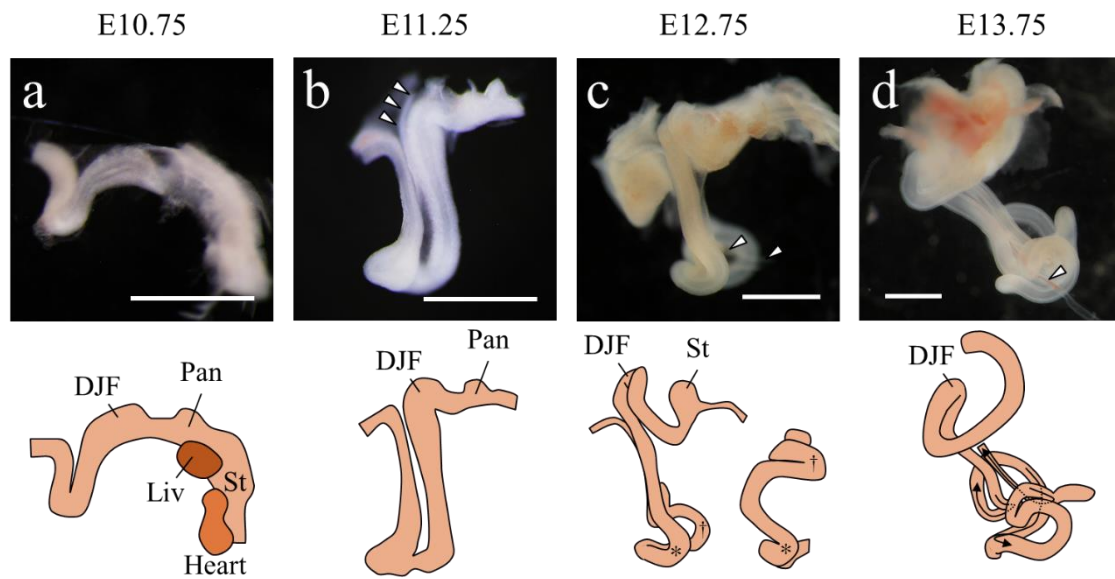


Figure 1-2. Gut morphology in prenatal mice.

(a) Whole-gut tube of the E 10.75 mouse with its sketch.

(b) Whole-gut tube of the E11.25 mouse with its sketch.

(c) Whole-gut tube of the E12.75 mouse with its sketches. The left sketch shows a whole-view of the gut tube, and the right shows the herniation part observed from the ventral side. Each * and † indicate the same flexure between the left and right sketches.

(d) Whole-gut tube of the E13.75 mouse with its sketch. Arrows indicate the running direction of the gut tube.

Arrowheads, cranial mesenteric artery; bars, 1 mm; DJF, duodenojejunal flexure; Liv, liver; Pan, pancreas bud; St, stomach.

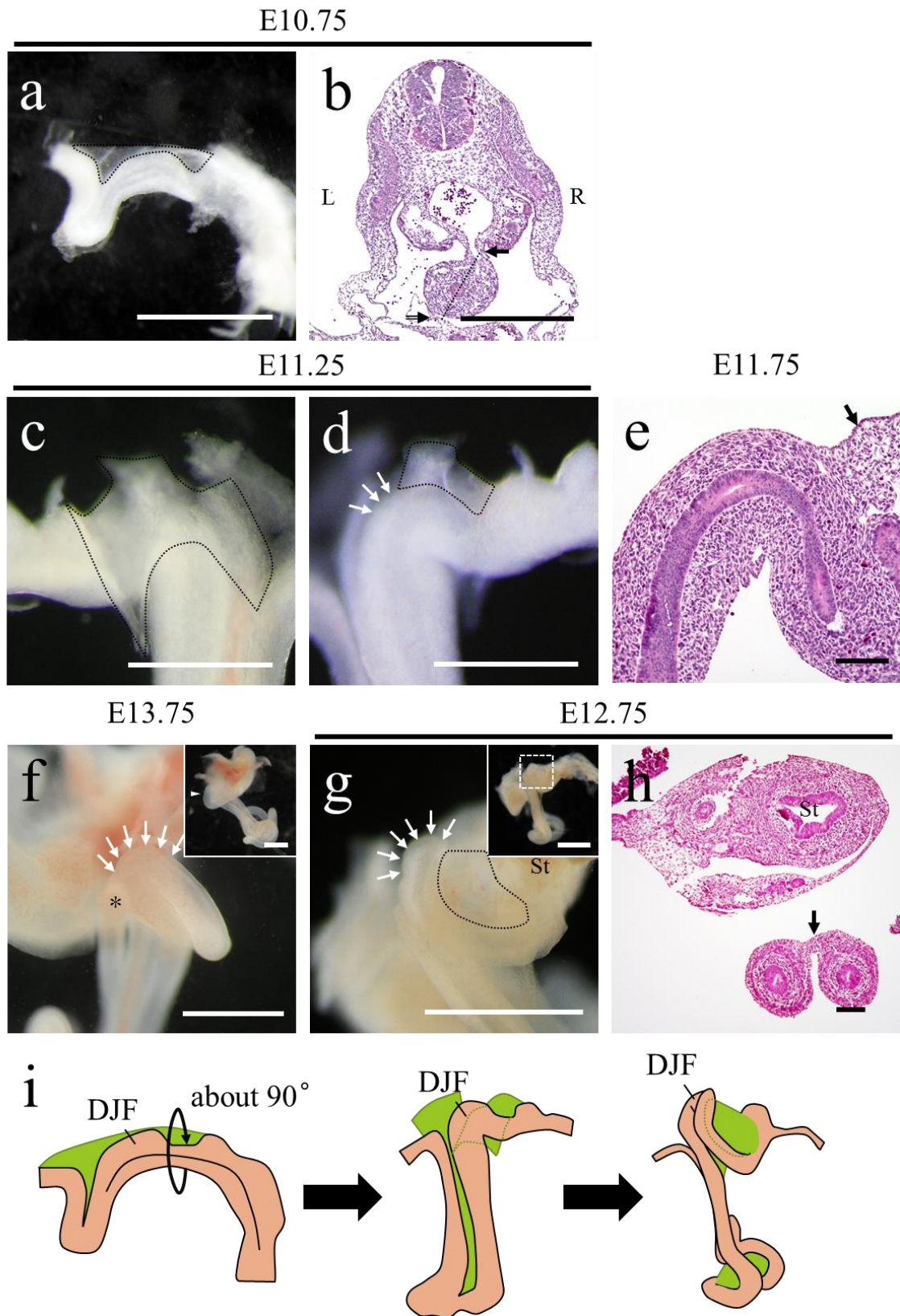


Figure 1-3. Attaching portion of the dorsal mesentery during mouse duodenojejunal flexure (DJF) formation.

(a and b) Attaching portion of the dorsal mesentery at E10.75 (expansion stage) in the whole-gut tube (a) and in a cross-section of the gut tube at the portion of the DJF (b). Bars, 1 mm (a) and 0.25 mm (b); dotted straight line, dorsal-ventral intestinal axis; double lined arrow, ventral mesentery; L, left side of the body axis; R, right side of the body axis.

(c-e) Attaching portion of the dorsal mesentery at E11.25–E11.75. (c) and (d) are high magnification views of the DJF at E11.25 observed from the left side (c) and the right side (d) of the body. (e) is a sagittal-section of the DJF at E11.75. Bars, 0.5 mm (c and d) and 100 μ m (e).

(f-h) Attaching portion of the dorsal mesentery at E12.75–E13.75. (f) and (g) are high magnification views of the DJF at E13.75 and E12.75, respectively. Each inset in (f) and (g) showed the whole-gut tube, and the arrowhead and white box respectively indicate the observing direction and observing position. (h) is a cross-section of the DJF at E12.75. Bars, 1 mm (f and g) and 100 μ m (h); St, stomach; *, lumen of the hindgut.

Black arrows, dorsal mesentery; dotted lines, outline of the dorsal mesentery; white arrows, outline of the DJF without the dorsal mesentery.

(i) Schema of the attaching portion of the dorsal mesentery during DJF formation. The dorsal mesentery is indicated as the green area. The DJF rotates in about 90° around the cranial-caudal intestinal axis indicated as the black line.

Chapter 2

Histological features

of the mouse fetal duodenojejunal flexure

Introduction

As the mechanism of flexure formation in the jejunum, the cooperation between the gut and dorsal mesentery is needed (Savin et al., 2011). However, in Chapter 1, the author suggested that the mechanism of mouse DJF formation was different from that of flexure formation in the jejunum and that the DJF was useful as a flexure formation model for the analysis of a novel mechanism.

In particular, for gut development, some biological processes including planar cell polarity (PCP), convergent extension (CE), and cell proliferation contributes to the dynamic morphological changes (Reed et al., 2009; Yamada et al., 2010; Mao et al., 2010). PCP is the plane polarity in the alignment of a collection of cells within a cell sheet (Jones and Chen, 2007) and needed for CE occurring during gut morphogenesis (Wallingford et al., 2002; Reed et al., 2009; Yamada et al., 2010). Briefly, CE is a morphogenetic process in which a cell sheet converges (narrows) along one axis and extends (elongates) along a perpendicular axis by cellular movements; polarized cell migration, cell shape change, and cell rearrangement (Wallingford et al., 2002). In *Xenopus*, the endoderm CE was reported as an important process in the gut tube elongation (Reed et al., 2009). In addition, the cell proliferation is also needed for gut morphogenesis including elongation and thickening of the gut tube.

In addition, some parts of the mechanisms could be shared with other organ morphogenesis including cardiac looping (Burn and Hill, 2009). During cardiac looping, the asymmetric morphologies including cell size, proliferation and

arrangement between the inner and outer curvatures are reported as the physical mechanisms (Shiraishi et al., 1992; Soufan et al., 2006).

In this chapter, the author focused on the mouse DJF as the model for a novel flexure formation mechanism and performed histological analyses to investigate specific morphologies in the mouse DJF. The author revealed several asymmetric morphologies between the inner and outer bending sides of the mouse DJF. The results suggested that these asymmetric morphologies contributed to asymmetric gut elongation along the cranial-caudal intestinal axis between the inner and outer bending sides to complete mouse DJF formation.

Materials and Methods

Ethics Statement

All animal experimentations in Chapter 2 were performed as described in Chapter 1. Some pregnant mice were injected intraperitoneally with Bromodeoxyuridine (BrdU) (Wako, Osaka, Japan) at 10 mg/10 g body weight 2 hours before being sacrificed.

Animals and Sample Preparations

Experimental animals were handled and sacrificed as shown in Chapter 1. B6 fetal mice at E10.75–E11.75 were used for subsequent analyses. The author defined fetal mice at E10.75 and E11.25–E11.75 as the pre-formation stage (the expansion stage as described in Chapter 1) and the post-formation stage (the flexure formation stage as described in Chapter 1), respectively. Whole embryos and dissected gut tubes were used at the pre-formation and post-formation stages, respectively. These tissues were fixed with 4% PFA in 0.1 M PB (pH 7.4) at 4°C overnight and embedded in 1% agarose gel before embedding in paraffin to ensure the exact angle and face of slicing. A part of the gut tubes at the post-formation stage was fixed with 3% glutaraldehyde in 0.1 M sodium cacodylate buffer (CB; pH 7.2) at 4°C for 4 hours.

Preparations for Histological Analyses

To investigate the DJF, cross- and sagittal-sections (semi-serial, 3- μ m-thick)

of the guts were prepared at the pre-formation and post-formation stages, respectively. At the pre-formation stage, the DJF was defined as the region located at the caudal position of the pancreatic buds and attached to the dorsal and ventral mesenteries, and the inner-outer bending axis was defined as the left-right intestinal axis according to Chapter 1. At the post-formation stage, the author selected the gut section showing a clear and distinct mucosal epithelium. These definitions of the DJF in histological analyses were also applied to subsequent histochemical and histoplanimetric analyses.

To investigate the cell morphology in the mesenchymal area of the DJF at the post-formation stage, the gut tubes fixed by 3% glutaraldehyde were post-fixed with 1% osmium tetroxide in 0.1 M CB at 4°C for 2 hours, dehydrated in increasing concentrations of ethanol, and embedded in epoxy resin (Quetol 812 Mixture; Nisshin EM, Tokyo, Japan). Semi-thin sagittal-sections (0.5- μ m-thick) of the gut tubes were stained with 1% Toluidine Blue. The cell shape in the mesenchymal area of the DJF was compared between the inner and outer bending sides of the DJF and corresponding sides in straight parts of the midgut. Ultra-thin sagittal-sections (70-nm-thick) of the DJF were double-stained with uranyl acetate and lead citrate and evaluated with a JEOL transmission electron microscope (TEM; JEM-1400plus; JEOL; Tokyo, Japan).

Histological Analyses and Histoplanimetry

The histological features of the gut tube were observed using the HE stained

cross- and sagittal-semi-serial sections of the DJF at the pre-formation and post-formation stages.

At the pre-formation stage, the total number and size of the mesenchymal cell nuclei were evaluated in the mesothelial area of the gut wall (Fig. 2-1a). Briefly, the measured area in the gut wall was a semi-square located in the range of 40 μm from the center of the inner-outer bending axis and 20 μm beneath the mesothelium perpendicular to the bending axis, and the inner long boundary of the measured area was parallel to the gut outline (Fig. 2-1a). This histoplanimetry was performed in the both inner and outer definite areas. Three HE stained semi-serial sections for each five embryo were observed, and the average in the three sections was expressed as the individual value.

At the post-formation stage, one section having the outer and inner sides of the mucosal epithelium clearly separated from each other was selected for this analysis. Based on the bending axis crossing the apexes of the extensor and flexor sides of the DJF, the gut wall thicknesses of the inner and outer bending sides of the DJF were measured with ImageJ (NIH, Bethesda, MD, USA) (Fig. 2-1b). The each value of the thickness was divided by the gut diameter, and expressed as percentage. The average of five embryos was compared between the outer and inner bending sides of the DJF. In addition, the nuclear height/width ratios of the mesothelial cells were measured at the apexes of the DJF at the inner and outer bending sides using ImageJ, and expressed by percentage (Fig. 2-1b). The author defined the height and width as the direction of the bending axis and its

perpendicular axis, respectively. The five adjacent mesothelial cells were measured (Fig. 2-1b), and the average value of the five cells was considered as the individual value. The average of five embryos was compared between the outer and inner bending sides of the DJF.

Immunohistochemical Analysis

Immunostaining for BrdU was performed in the pre-formation and post-formation stage DJFs according to the following procedure. The paraffin series sections were deparaffinized and incubated in citrate buffer (pH 6.0) for 20 min at 105°C for antigen retrieval. After cooling, the sections were treated with methanol containing 0.3% H₂O₂ for 20 min at room temperature (RT) to remove internal peroxidase. After being washed in phosphate-buffered saline (PBS), the sections were blocked by 10% normal goat serum for 60 min at RT. Then, the sections were incubated with rat monoclonal anti-BrdU antibodies (1:200, Abcam, Cambridge, UK) overnight at 4°C. After 3 times of washing in PBS, the sections were incubated with biotin-conjugated goat anti-rat IgG antibodies for BrdU (1:100, Caltag, London, UK) for 30 min at RT, washed again, and incubated with streptavidin-biotin complex (SABPO® kit, Nichirei, Tokyo, Japan) for 30 min at RT. The section were incubated with 3,3'-diaminobenzidine tetrahydrochloride (DAB)-H₂O₂ solution. Finally, the sections were counterstained with hematoxylin.

Cell proliferation were analyzed by using the BrdU-immunostained DJF sections. At the pre-formation stage, the number of total nuclei and BrdU-positive nuclei of the

mesenchymal cells were counted in four mesenchymal areas: the dorsal, ventral, inner, and outer areas (Fig. 2-1a). The long boundaries of the measured regions were along the dorsal-ventral intestinal axis or inner-outer bending axis, and the short boundaries of measured regions were same with the diameter of the gut mucosa (Fig. 2-1a). The BrdU-positive nuclei/total nuclei were expressed as the percentage of BrdU-positive nuclei. The three sections of each embryo were measured, and the average of the three sections was considered as an individual value. The average of four embryos was compared among the each side.

At the post-formation stage, the number of total nuclei and BrdU-positive nuclei of the mesenchymal cells were counted in the inner and outer bending sides of the mesenchymal area, and the measured regions were located in the range of 25 μm from the center of the bending axis (Fig. 2-1b). The percentage of BrdU-positive nuclei was calculated as in the pre-formation stage, and the average of four embryos was compared between the inner and outer bending sides.

Cell Morphological Analysis

At the post-formation stage, sagittal-sections were prepared from dissected gut tubes embedded in epoxy resin. The cell morphologies in the mesenchymal area were compared between the inner and outer bending sides of the DJF, and these differences were quantitatively evaluated (Fig. 2-1c). Briefly, the inner-outer bending axis crossing the extensor and flexor sides of the DJF was defined in digital images, and the long and short lengths of each cell on the line of the inner-outer bending axis were measured using

ImageJ (Fig. 2-1c). The value of the long length was divided by that of the short length to calculate the long/short length ratio (Fig. 2-1c). The averages of the long and short lengths and the long/short length ratio of each cell (≥ 20 cells) were calculated from one gut tube and defined as an individual value. In addition, the direction of each cell against the inner-outer bending axis was also quantified (Fig. 2-1c). The angle between the inner-outer bending axis and the direction of the long length of each cell was also measured from 1 gut tube, and each proportion of cell number in $0^\circ \leq \text{the angle} \leq 30^\circ$, $30^\circ < \text{the angle} \leq 60^\circ$, and $60^\circ < \text{the angle} \leq 90^\circ$ was calculated (Fig. 2-1c). These averages of five gut tubes were compared between the inner and outer bending sides of the DJF. These histoplanimetric parameters in the inner and outer bending sides of the DJF were also compared between the corresponding two sides of the straight parts of the midgut adjacent to the DJF, as a comparative control (Fig. 2-1c).

To investigate the asymmetry in the adherens junction between the inner and outer bending sides of the DJF, ultra-thin sagittal-sections (70-nm-thick) of the DJF were evaluated. The author counted the number of adherens junctions per cell and measured the length by ImageJ software (NIH; Bethesda, MD, USA). The averages of fifty cells in each of five embryos were compared between the inner and outer bending sides.

Statistical Analysis

The results were expressed as mean \pm standard error (SE) and analyzed by Wilcoxon test ($P < 0.05$) or paired *t*-test ($P < 0.05$).

Results

Histological Features of the Mouse DJF at the Pre-formation Stage

At the pre-formation stage, in order to find out histological differences of the DJF, the cross sections of the DJF were observed (Fig. 2-2). The mucosal layer of the DJF was lined by the simple columnar epithelium, and the outer layer of the mucosa was composed by the round shape mesenchymal cells having narrow cytoplasm (Fig. 2-2a). The outermost layer of the DJF was covered by the mesothelium continuing from the dorsal and ventral mesenteries (Figs. 2-2a–c). In the morphological feature of these cells, although no constant difference was observed in the mesenchymal cells around the mucosa (Fig. 2-2a), the cells in the mesothelial area of the gut wall seemed to be larger in the inner side of the DJF than in the outer side (Figs. 2-2b and c). Therefore, the author compared the nuclear number and the nuclear size between the inner and outer bending sides of the DJF as the indices for the number of cells and each cell size, respectively (Figs. 2-2d and e). In the nuclear number, there was no difference between the inner and outer measured areas (Fig. 2-2d). In the nuclear size, the inner side of the DJF showed higher values than the outer side (Fig. 2-2e).

Furthermore, the contribution of cell proliferation to DJF formation was assessed at the pre-formation stage (Figs. 2-2f–h). The number of BrdU-positive mesenchymal cells in the mesenchymal area was examined as the percentage of positive nuclei in the dorsal, ventral, inner, and outer areas (Fig. 2-2f). The inner definite area showed the highest value and had significantly higher values than the

dorsal or ventral area (Fig. 2-2g). The summation values of the inner and outer areas tended to be higher than those of the dorsal and ventral areas (Fig. 2-2h).

Histological Features of the Mouse DJF at the Post-formation Stage

At the post-formation stage, the sagittal-sections of the DJF were observed (Fig. 2-3). The mucosal layer of the DJF was also the simple columnar epithelium, and the surrounding mesenchymal layer was composed by the slender shape mesenchymal cells showing the longitudinal axis (Figs. 2-3a–c). The gut wall in the outer side of the DJF was thinner than that in the inner side (Figs. 2-3a), and a significant difference was demonstrated in histoplanimetry (Fig. 2-3d). Furthermore, the shape of the mesothelium lining the outermost DJF was squamous in the outer bending side (Fig. 2-3b), but that was cuboidal or round in the inner bending side (Fig. 2-3c). According to this observation, the nuclear height/width ratio of the mesothelium was significantly lower in the outer side than in the inner side (Fig. 2-3e). For the cell proliferation assay, the outer side of the DJF had more abundant BrdU-positive mesenchymal cells than the inner side (Fig. 2-3f), and a significant difference was demonstrated in the measurement of BrdU-positive nuclei (Fig. 2-3g).

To investigate the mesenchymal cell shapes of the post-formation stage DJF, semi-thin sections were observed (Fig. 2-4). The mesenchymal cells showed large nuclei and narrow cytoplasm, and individual cells were clearly separated (Figs. 2-4a–c). As described above, the cell shape of the mesothelium surrounding the DJF differed between the inner and outer bending sides (Fig. 2-4a). Similarly, in the mesenchymal area of the

DJF, the cells in the outer side were longer along the perpendicular direction to the inner-outer bending axis (Fig. 2-4b), while those in the inner side were longer along the inner-outer bending axis (Fig. 2-4c). At the straight midgut subsequent to the DJF (Fig. 2-5), no morphological asymmetry of the mesenchymal cells was observed between the two sides corresponding to the inner and outer bending sides of the DJF (Figs. 2-5a–c).

To quantitatively evaluate the shape and direction of the mesenchymal cells, the following histoplanimetry was performed: the long and short lengths, the long/short length ratio, and the angle between the inner-outer bending axis and the longitudinal axis of each mesenchymal cell (See Fig. 2-1c). The long length of each cell was significantly longer in the outer side of the DJF than in the inner side, while the short length showed no difference between both sides (Fig. 2-4d). Therefore, the long/short length ratio was significantly higher in the outer side than in the inner side (Fig. 2-4d). In addition, the proportion of cell number in each range of the angle revealed that cells in the range of $0^\circ \leq \text{the angle} \leq 30^\circ$ were significantly more abundant in the inner side of the DJF than in the outer side and that cells in the range of $60^\circ < \text{the angle} \leq 90^\circ$ were significantly more abundant in the outer side than in the inner side (Fig. 2-4e). These results demonstrate that the longitudinal axis of most of the cells in the inner side of the DJF were parallel to the inner-outer bending axis and those in the outer side were perpendicular to the bending axis. No significant difference was detected between both corresponding sides in the mesenchymal area of the straight midgut part (Fig. 2-5d and e).

Fig. 2-6 shows the ultrastructures of mesenchymal cells in the DJF. Each mesenchymal cell had a large nucleus and narrow cytoplasm, which was filled with many

ribosomes, and no remarkable asymmetry was noted in the intracellular organelles in the cytoplasm of the mesenchymal cells in the inner and outer bending sides of the DJF (Figs. 2-6a–d). However, the intercellular spaces between each mesenchymal cell were narrower in the inner side of the DJF (Fig. 2-6a) compared with the outer side (Fig. 2-6b). The inner side was more crowded with mesenchymal cells than the outer side, and the longitudinal axes of these cells were arranged along the inner-outer bending axis (Fig. 2-6a). Conversely, the mesenchymal cells of the outer side tended to be elongated along the perpendicular direction to the inner-outer axis, and some of them displayed a round shape (Fig. 2-6b). Furthermore, the mesenchymal cells in the inner side exhibited only a few cytoplasmic processes and close intercellular contact via adherens junctions (AJs) (Figs. 2-6a and c). In contrast, the mesenchymal cells in the outer side displayed many cytoplasmic processes that were connected with other cells via AJs (Figs. 2-6b and d). To quantify the morphological features of the AJs, the number of AJs per cell (Fig. 2-6e) and the lengths of one AJ (Fig. 2-6f) were compared between the inner and outer bending sides. These results show that there were significantly fewer and longer AJs in the inner side than in the outer side (Figs. 2-6e and f).

Discussion

In this chapter, the author found several asymmetric morphologies between the inner and outer bending sides of the mouse DJF. The author suggests that these asymmetric morphologies are related to mouse DJF formation. In general, as the mechanisms for asymmetric morphogenesis, differential cell proliferation, migration and adhesion are considered (Levin, 2005).

At the pre-formation stage, the nuclear size of the mesenchymal cells in the mesothelial area of the DJF gut wall were larger in the future inner side than in the future outer side, despite of the same cell density in the both sides. These results indicated the asymmetric morphology of the mesenchymal cells in the cell size or cell polarity. During chick cardiac looping, it has been reported that the more increase of cell size was observed in the outer curvature than in the inner curvature (Soufan et al., 2006). However, the result of the cell size in the developing DJF was the opposite one that the size was larger in the inner side than in the outer side of the DJF. In addition, although the mesenchymal cells at the pre-formation stage were round shapes, the cells at the post-formation stage had clear polarity. Therefore, the author suggests that the cells in the future inner side start to be long along the apico-basal intestinal axis, and the cells in the future outer side start to be long along the cranial-caudal intestinal axis. In addition, more active cell proliferation is observed along the inner-outer bending axis than the dorsal-ventral intestinal axis at the pre-formation stage. These results indicated that the mesenchymal proliferations with the asymmetric cell morphology along the inner-outer bending axis at the pre-formation stage cause the expansion of the DJF along the bending axis to be a force to DJF formation.

Cell proliferation followed by the morphological change is usual in organogenesis including cardiac looping (Soufan et al., 2006).

Furthermore, at the post-formation stage, although the cell proliferation rate was higher in the outer side of the DJF than in the inner side, the outer side had the thinner gut wall than the inner side. From this finding, the author considered that the gut wall in the outer side of the DJF had more capacity to elongate along the cranial-caudal intestinal axis than that in the inner side. In *Xenopus*, gut looping is also related to differential elongation between the left and right sides of the gut tube, suggesting differential CE (Muller et al., 2003). Therefore, CE along the cranial-caudal intestinal axis would occur more frequently in the outer side than in the inner side of the DJF.

Since the establishment of cell polarity is required for CE (Wallingford et al., 2002), the author investigated the cell polarity between the inner and outer bending sides of the DJF and revealed its asymmetric morphology. At the post-formation stage, the mesothelium of the outer side was more squamous than that of the inner side in the DJF. In addition, mesenchymal cell shape in the mesenchymal area was different between the inner and outer bending sides; the cells in the outer side were longer than those in the inner side. Moreover, the mesenchymal cells were elongated along the inner-outer bending axis in the inner side of the DJF and were elongated along the perpendicular direction to the inner-outer axis in the outer side of the DJF. These differences in shape and direction of the mesenchymal cells are considered characteristics of the DJF morphology. Differential cell arrangement is also observed between the inner and outer curvatures during cardiac looping (Shiraishi et al., 1992). Thus, differential cell polarity

between the inner and outer bending sides would be related to DJF formation.

In TEM observations, the mesenchymal cells in the inner side were crowded yet well-ordered along the inner-outer bending axis, and adjoined by a few long AJs. In contrast, the mesenchymal cells in the outer side were disordered and developed cytoplasmic processes in the intercellular spaces, and these processes were connected by abundant and short AJs. Since the similar asymmetric morphology is reported in the tilting dorsal mesentery showing the asymmetric length between the left and right sides (Davis et al. 2008; Welsh et al. 2013), the author also suggest that the morphological features of the mesenchymal cells in the outer side would be more suitable for spreading than those in the inner side for asymmetric elongation.

Therefore, the author hypothesized that the mesenchymal cells in the outer side elongate via CE along the perpendicular direction to the inner-outer bending axis more efficiently than those in the inner side due to asymmetric cell shape, direction and proliferation, and these asymmetries might contribute to the formation of the mouse DJF.

In summary, the author proposed the process of mouse DJF formation as shown in Fig. 2-7. Briefly, at the pre-formation stage, the mesenchymal cells in the mesenchymal area proliferate and accumulate to expand the DJF along the future inner-outer bending axis, and these accumulated cells contribute as a force of DJF formation. At the post-formation stage, the differences in the cell proliferation rate and mesenchymal cell morphology between the inner and outer bending sides also contribute to the asymmetric elongation of the gut wall via CE as the other force of DJF formation. Finally, the DJF accomplish its bending.

As described in Chapter 1, the mouse DJF formed with the 90° counterclockwise rotation along the cranial-caudal intestinal axis during the pre-formation stage to the post-formation stage. The author clarified that the left and right sides of the DJF based on the intestinal axis became the future inner and outer bending sides, respectively. Therefore, it was considered that the asymmetric development of the DJF along the left-right intestinal axis contributed to DJF formation. It is well known that the left-right asymmetric morphologies are concerned with various internal organs including the gastrointestinal tract (Levin, 2005). In gut development, the left-right asymmetric morphology in the dorsal mesentery determines the direction of gut rotation (Davis et al. 2008; Kurpios et al. 2008; Welsh et al. 2013). Interestingly, the author found that several asymmetric morphologies in the mouse DJF observed in this study were similar to those in the dorsal mesentery: the characteristics of the asymmetric morphology in the DJF, for example. In the dorsal mesentery tilting leftward, crowded cells in the left side formed contacts between adjacent cells via their plasma membranes, while scattered cells in the right side formed intercellular junctions via filopodia (Davis et al. 2008; Welsh et al. 2013). These researchers suggest that the asymmetric extracellular matrix (ECM) distribution in the dorsal mesentery is necessary for the establishment of those left-right asymmetric morphologies in the dorsal mesentery (Kurpios et al. 2008). Therefore, the author suggests that the mechanism under the asymmetric morphologies should be similar with that in other organogenesis showing the left-right asymmetry.

In conclusion, the developing mouse DJF showed asymmetric morphologies between the inner and outer bending sides. The author considered that these asymmetric

morphologies were necessary for the asymmetric elongation rate along the cranial-caudal intestinal axis between the inner and outer bending sides to complete mouse DJF bending. The author suggests that mouse DJF formation is one of the phenomena of left-right asymmetry.

Summary

In Chapter 1, the author revealed the mouse DJF as a useful model for elucidating a novel mechanism of flexure formation. In this chapter, the author performed the histological analyses of the developing mouse DJF to elucidate its histological features related to flexure formation.

In the histological analyses of mouse DJF formation, the author found several asymmetric morphologies between the inner and outer bending sides of the DJF. At the pre-formation stage, the nuclei size of the mesenchymal cells in the mesothelial area was larger in the future inner side of the DJF than in the future outer side, while the cell density was not significantly different between the two sides. The proliferation rate in the DJF was higher along the future inner and outer bending axis than along its perpendicular axis. On the other hand, at the post-formation stage, the gut wall thickness was higher in the inner side of the DJF than in the outer side, while the proliferation rate was higher in the outer side than in the inner side. In the detail analyses of cell shapes, the cells in the inner side of the DJF were elongated along the inner-outer bending axis and had narrow intercellular spaces between the adjacent cells connecting with each other via a few longer AJs. The cells in the outer side of the DJF were elongated along the perpendicular direction to the inner-outer bending axis and had large intercellular spaces between the adjacent cells connecting with each other via abundant short AJs on the cytoplasmic processes.

Those differences in the mesenchymal cell morphology between the future inner and outer bending sides suggest the difference in CE rate between the two sides. The CE

difference contributes to the asymmetric elongation of the gut wall between the inner and outer bending sides as the force of mouse DJF formation. This morphological change is similar to that in other asymmetric organs.

Tables and Figures

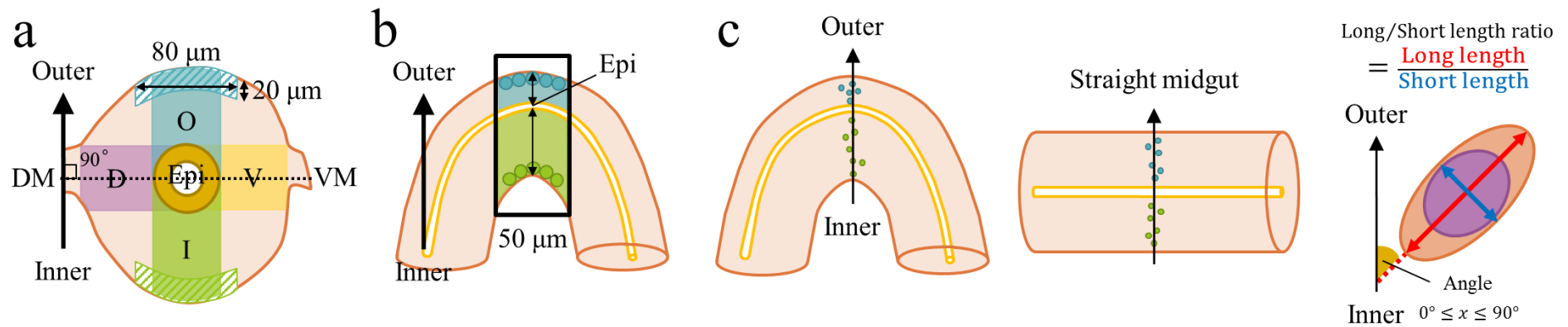
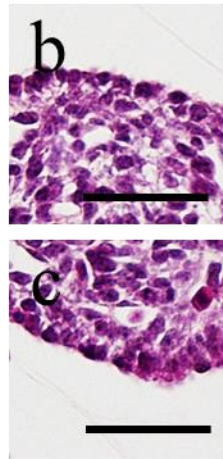
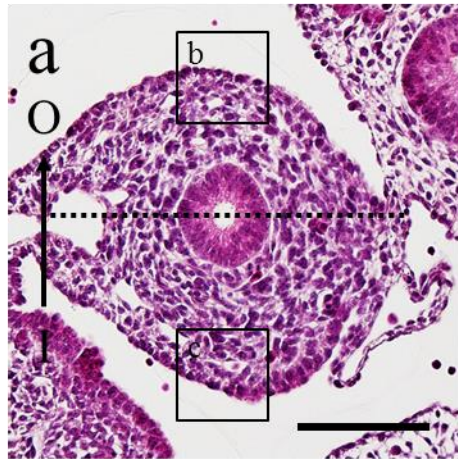


Figure 2-1. Methodologies for the histoplanimetry.

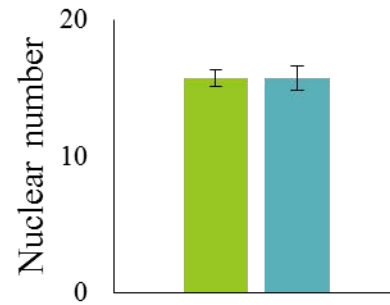
(a) Shema for the histoplanimetry at the pre-formation stage. In the cross-section, the dorsal-ventral intestinal axis is defined as the dotted line passing on the center of the lumen from the dorsal mesentery (DM) to the ventral mesentery (VM). The inner-outer bending axis is crossing at the right angle with the dorsal-ventral intestinal axis. The oblique areas in the inner and outer sides are used for the histoplanimetry of the mesenchymal cells, defined as a semi-square 80 μm long along the dorsal-ventral intestinal axis and 20 μm broad from the surface of the mesothelium along the inner-outer bending axis. The colored areas are used for the evaluation of the bromodeoxyuridine (BrdU)-positive nuclei: the dorsal (D), ventral (V), inner (I), and outer (O) areas. The long boundaries are along the dorsal-ventral intestinal axis or inner-outer bending axis, and the narrow boundaries are same with the diameter of the gut mucosal epithelial layer (Epi).

(b) Shema for the histoplanimetry at the post-formation stage. The double pointed arrows on the line crossing the apexes of the extensor and flexor sides are used for the histoplanimetry of the gut wall thickness. The box 50 μm wide is the area for the evaluation of the BrdU-positive nuclei. The circles in each side indicate cells used for the histoplanimetry of the mesothelial cells.

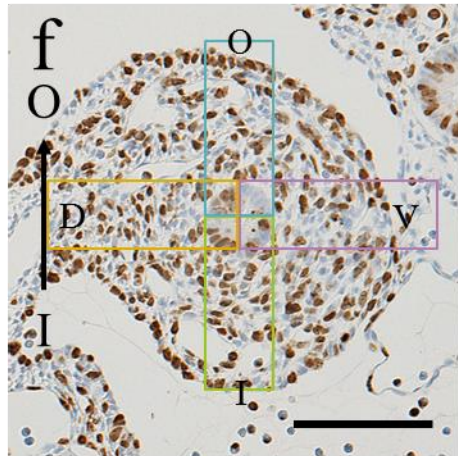
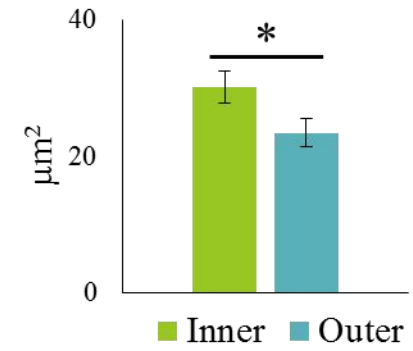
(c) Schema of the long and short length and the angle of the direction of the cell longitudinal axis against the inner-outer bending axis in the DJF and straight midgut.



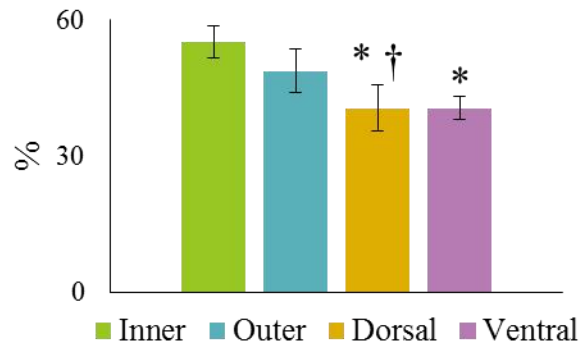
d Nuclear number



e Nuclear size



g BrdU-positive ratio



h BrdU-positive ratio

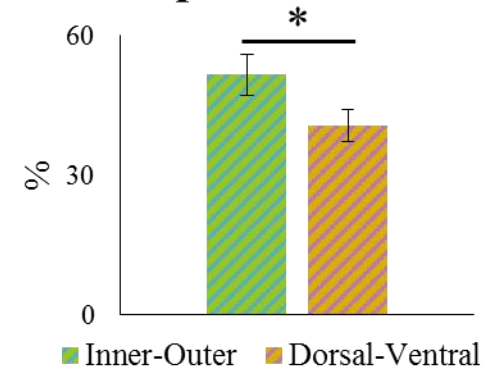


Figure 2-2. Histological differences between the predicted inner and outer bending sides of the mouse duodenojejunal flexure (DJF) at the pre-formation stage.

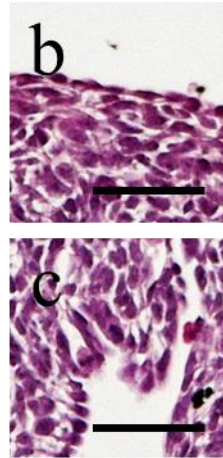
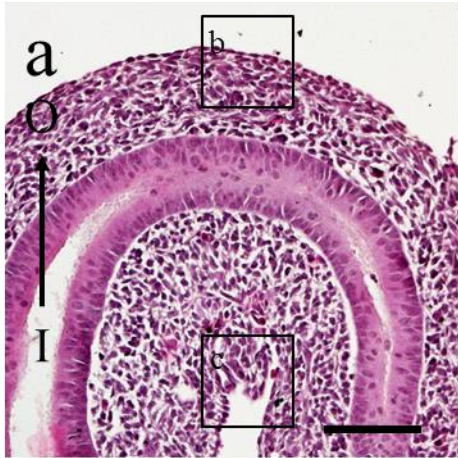
(a) Hematoxylin-eosin stained cross-section of the DJF. The dotted line indicates the dorsal-ventral intestinal axis. Bar, 100 μm .

(b and c) High magnification views of (a). Bars, 50 μm .

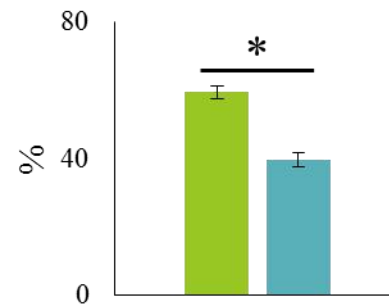
(d and e) Comparison of the nuclear number and size of the mesenchymal cells in the mesothelial area of the inner and outer bending sides of the DJF. Values = mean \pm standard error (SE); n = 5; *, significant difference between the inner and outer areas (Wilcoxon test, $P < 0.05$).

(f) Immunohistochemistry for bromodeoxyuridine (BrdU) of the DJF. Each box indicates the measured area for the dorsal (D), ventral (V), inner (I), and outer (O) sides. Bar, 100 μm .

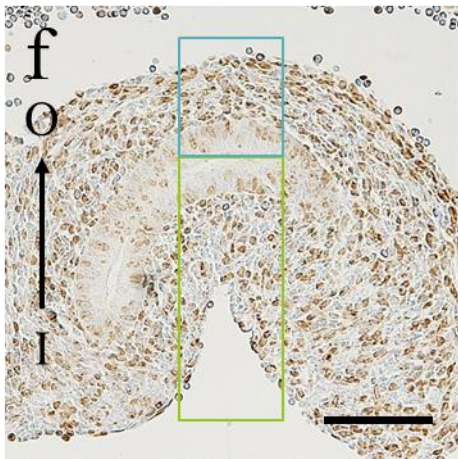
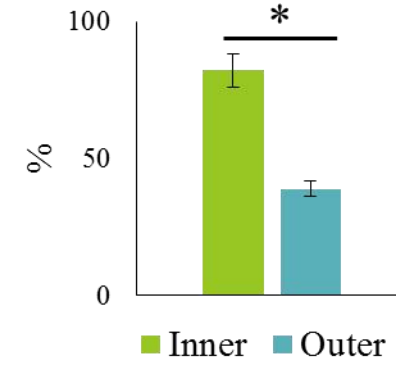
(g and h) Comparison of the percentage of the BrdU-positive nuclei in the mesenchyme. (g) compares the dorsal, ventral, inner, and outer areas. n = 4; *, significant difference against the inner side (paired t -test, $P < 0.05$); †, significant difference against the outer side (paired t -test, $P < 0.05$). (h) compares the dorsal-ventral and inner-outer areas. Values = mean \pm SE; n = 4; *, significant difference between the each column (paired t -test, $P < 0.05$).



d Wall thickness



e Nuclear shape



g BrdU-positive ratio

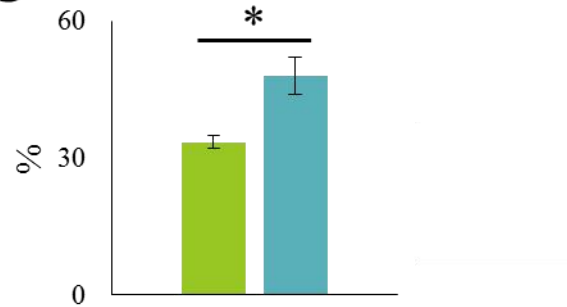


Figure 2-3. Histological differences between the inner and outer bending sides of the mouse duodenojejunal flexure (DJF) at the post-formation stage.

(a) Hematoxylin-eosin stained cross-section of the DJF. The dotted line indicates the dorsal-ventral intestinal axis. Bar, 100 μm .

(b and c) High magnification views of (a). Bars, 50 μm .

(d and e) Comparison of the gut wall thickness and the nuclear shape of the mesothelial cells of the DJF. Values = mean \pm standard error (SE); n = 5; *, significant difference between the inner and outer sides (Wilcoxon test, $P < 0.05$).

(f) Immunohistochemistry for bromodeoxyuridine (BrdU) of the DJF. Each box indicates the measured area for the inner (green), and outer (blue) sides. Bar, 100 μm ; I, inner side; O, outer side.

(g) Comparison of the percentage of the BrdU-positive nuclei in the mesenchyme. Values = mean \pm SE; n = 4; *, significant difference between the inner and outer sides (paired t -test, $P < 0.05$).

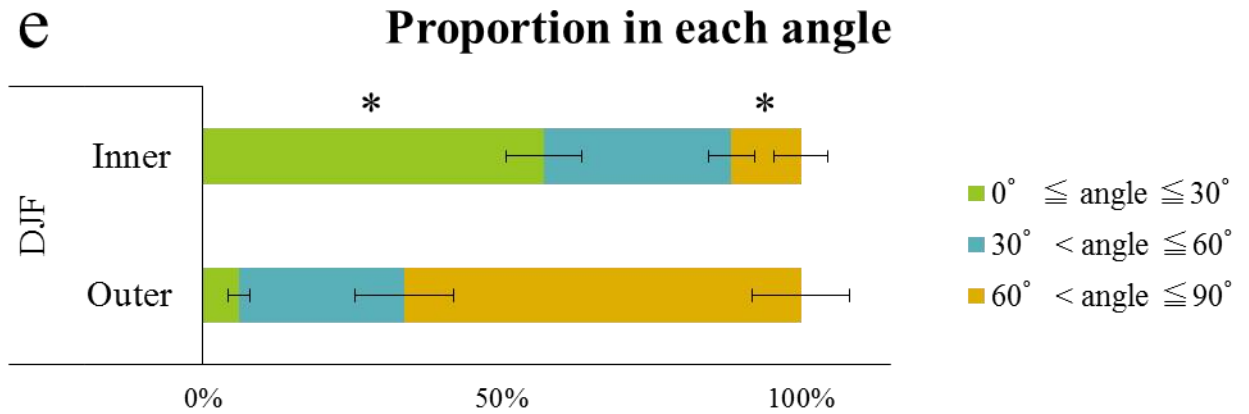
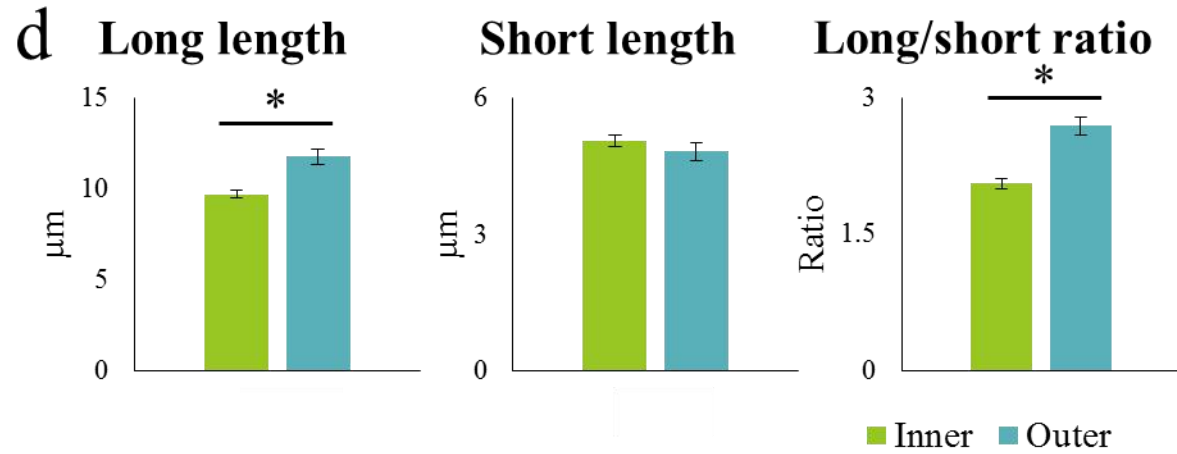
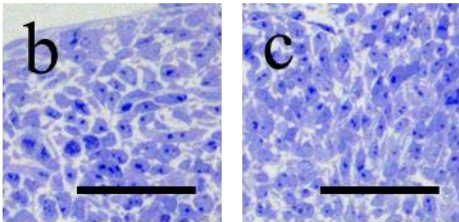
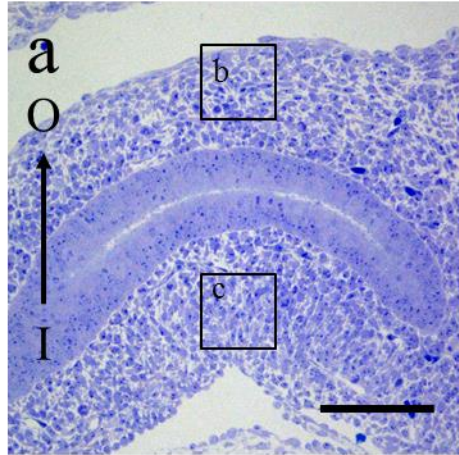


Figure 2-4. Morphological differences of the mesenchymal cell between the inner and outer bending sides of the duodenojejunal flexure (DJF) at the post-formation stage.

(a) Semi-thin section of the DJF. Bar, 100 μm ; I, inner side; O, outer side.

(b and c) High magnification views of (a). Bars, 50 μm .

(d) Comparison of the long length, short length, and long/short length ratio of the mesenchymal cells of the DJF.

(e) Comparison of the proportion of cells at angles between the inner-outer bending axis and the direction of the longitudinal axis of each cell within every 30° in the DJF. Values = mean \pm standard error; $n = 5$; *, significant difference between the inner and outer sides (Wilcoxon test, $P < 0.05$).

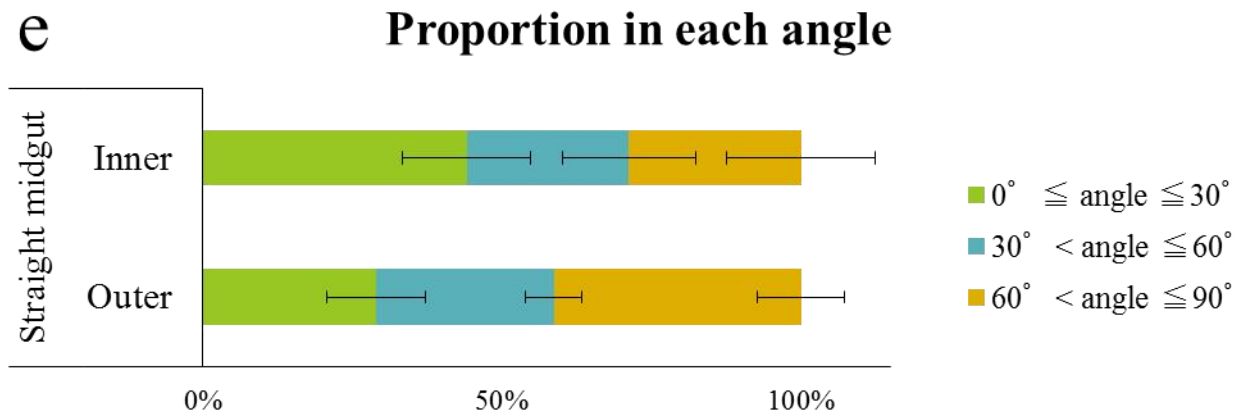
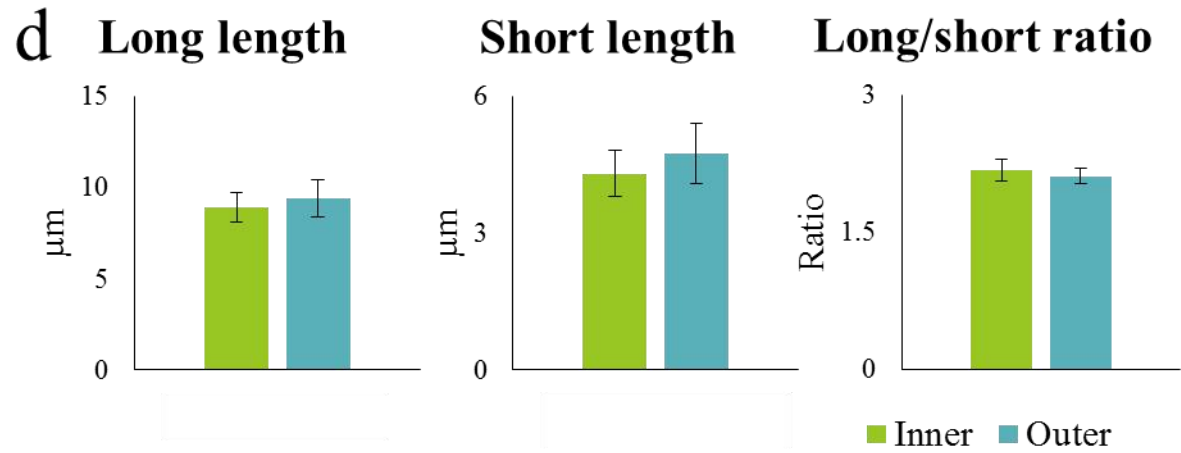
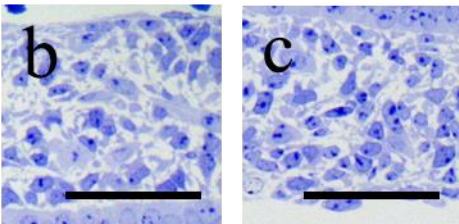
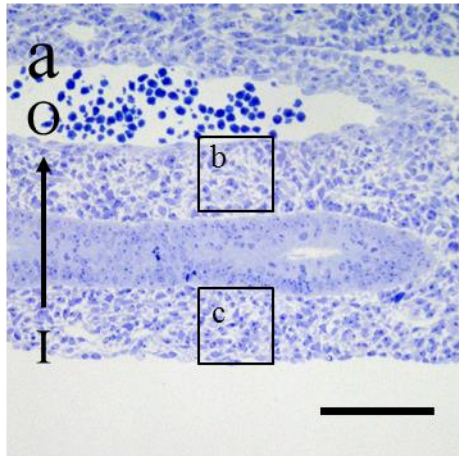


Figure 2-5. Morphology of the mesenchymal cell of the mouse straight midgut part at the post-formation stage.

(a) Semi-thin section of the straight midgut part. Bar, 100 μm ; I, side corresponding with the inner side of the duodenojejunal flexure (DJF); O, side corresponding with the outer side of the DJF.

(b and c) High magnification views of (a). Bars, 50 μm .

(d) Comparison of the long length, short length, and long/short length ratio of the mesenchymal cells of the straight midgut part.

(e) Comparison of the proportion of cells at angles between the inner-outer bending axis and the direction of the longitudinal axis of each cell within every 30° in the straight midgut part. Values = mean \pm standard error; n = 5.

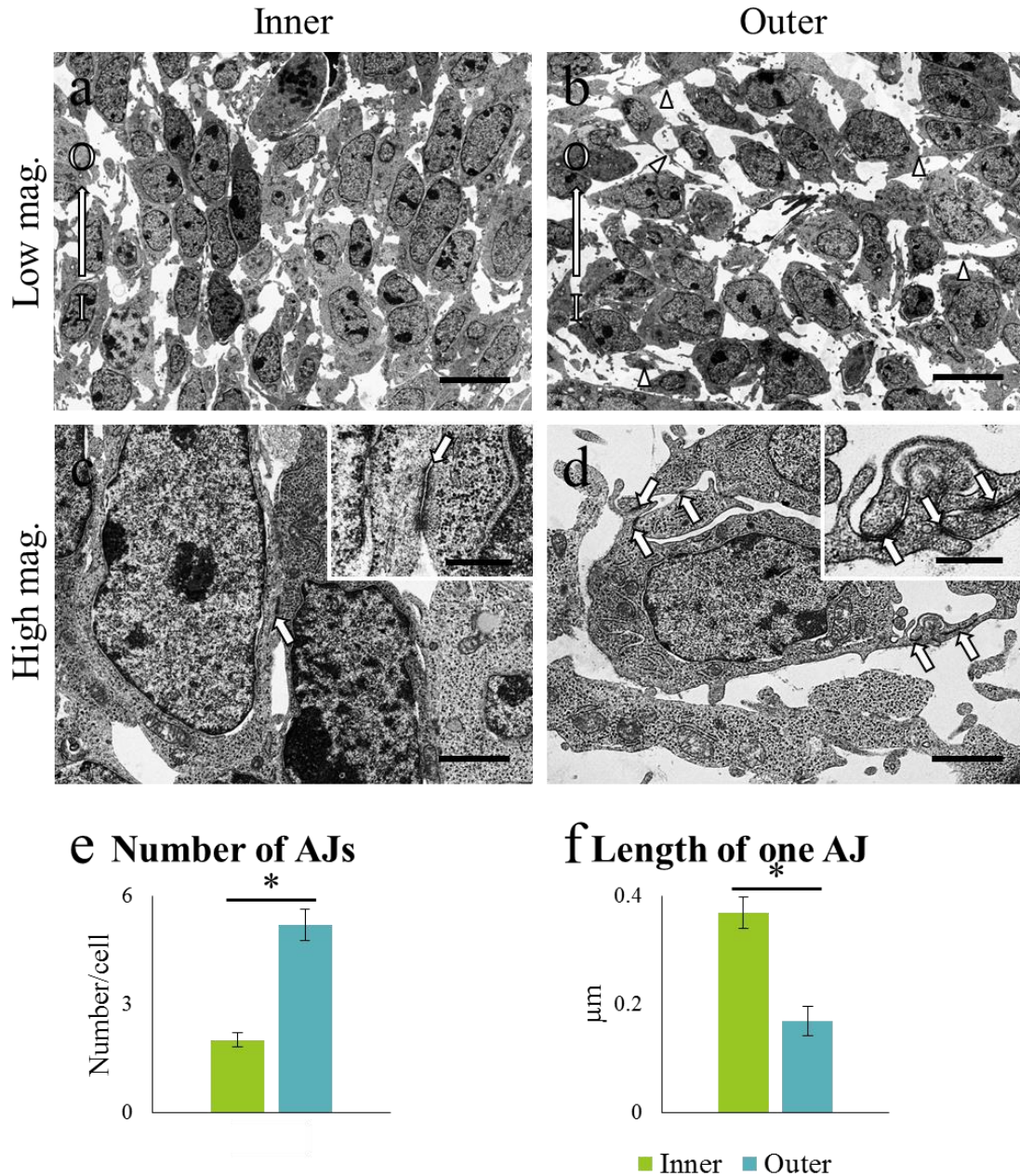


Figure 2-6. Ultrastructural differences of the mesenchymal cells between the inner and outer bending sides of the mouse duodenojejunal flexure (DJF) at the post-formation stage.

(a and b) Lower magnified views (Low mag.) of the mesenchymal cells in the inner (a) and outer (b) sides of the DJF. Arrowheads, cytoplasmic processes.

(c and d) Higher magnified views (High mag.) of the mesenchymal cells in the inner (c) and outer (d) sides of the DJF. Arrows, adherens junctions.

Bars, 10 μm (a and b), 2 μm (c and d), and 500 nm (insets); I, inner side; O, outer side. **(e and f)** Comparison of the number of adherens junctions (AJs) per a mesenchymal cell (e) and the length of one AJ (f) in the DJF. Values = mean ± standard error; n = 5; *, significant difference between the inner and outer side (Wilcoxon test, $P < 0.05$).

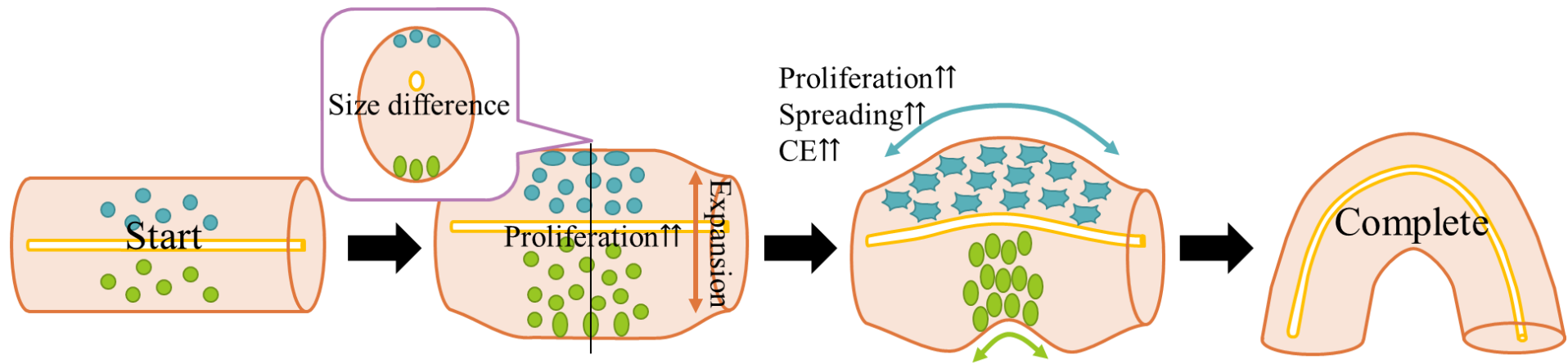


Figure 2-7. Proposed model of mouse duodenojejunal flexure (DJF) formation.

Blue circles, cells in the outer side; Green circles, cells in the inner side. The large black arrows indicate the flow of DJF formation. Based on the cooperation of cell proliferation and convergent extension (CE) with asymmetric mesenchymal cell morphology, the DJF accomplishes its formation.

Chapter 3

Asymmetric distribution

of the gut component cells and molecules observed

in the developing mouse duodenojejunal flexure

Introduction

In Chapter 2, the author clarified that the morphologies and proliferation rate of the mesenchymal cells differed between the inner and outer bending sides of the mouse DJF. Those asymmetries between the inner and outer bending sides would be necessary for mouse DJF formation. In this chapter, the author focused on the gut components including cells and ECM as the candidates to establish those asymmetries.

The developing gut contains cells derived from three germ layers: the endoderm (mucosal epithelium), mesoderm (mesenchymal cells, smooth muscle cells, vessels, and mesothelium), and ectoderm (neurons and glia). Those gut components affect the differentiation of each other and also the gut morphology. For example, the enteric neural crest cells, progenitors of neurons and glia, regulate the establishment and maintenance of stomach mesenchymal-epithelial patterning including smooth muscle development in chick (Faure et al., 2015). In addition, in human and chick, smooth muscle differentiation is needed for villi formation of the gut tube (Shyer et al., 2013).

On the other hand, the ECM is a component of the connective tissues and fibers, excluding cells. The ECM plays an important role, not only in structural support, but also in the control of cellular behavior such as survival, proliferation, differentiation, polarity, and migration (Hynes, 2009). During cell proliferation, several proteoglycans that contain heparin and heparan sulfate act as reservoirs of growth factors, such as fibroblast growth factors (FGF), transforming growth factor- β (TGF- β), bone morphogenetic proteins, and sonic hedgehog. Moreover, the distribution of proteoglycans provides growth factor gradients for patterning during development (Hynes, 2009). These proteoglycans are also

required for ligand reception and signal activation by FGF and TGF- β (Hynes, 2009; Shimokawa et al., 2011). In addition, ECM receptors, including integrins, acts as signal transducers, thus playing important roles in regulating cell behavior (Kim et al. 2011; Legate et al. 2009). Briefly, once ECM molecules connect to these receptors, the receptors activate several intracellular signaling pathways for cell proliferation, cell survival, cell shaping, and cell migration. Moreover, there exists a crosstalk between these ECM receptors and growth factor receptors which activate intracellular signaling pathways similar to those pathways that act the downstream of integrins (Kim et al. 2011; Legate et al. 2009). Interestingly, although the author suggested the similarity in the asymmetric morphologies between the DJF and the dorsal mesentery in Chapter 2, the dorsal mesentery shows asymmetric ECM distribution, suggesting that the ECM change is necessary for the establishment of the left-right asymmetric morphologies in the dorsal mesentery (Kurpios et al. 2008).

Therefore, in this chapter, the author compared the population and differentiation of the mouse DJF component cells derived from three germ layers and the distributions of ECM molecules between the inner and outer bending sides of the developing mouse DJF. The author revealed that neural differentiation and ECM distribution showed different between the inner and outer bending sides of the mouse DJF, suggesting their contribution for the establishment of asymmetric morphologies in mouse DJF formation.

Materials and Methods

Ethics Statement

All animal experimentations in Chapter 3 were performed as described in Chapter 1.

Animals and Sample Preparations

Experimental animals were handled as shown in Chapter 1. Embryos aged E10.75 (pre-formation stage) and E11.25–E 11.75 (post-formation stage) were used for subsequent analyses. The procedures of sample treatment were shown in Chapter 2.

Preparations for Histological Analyses

Cross- and sagittal-paraffin sections (semi-serial, 3- μ m-thick) of the gut tubes were prepared for the following analyses at the pre-formation and post-formation stages, respectively. Details of the procedures are described in Chapter 2.

Immunohistochemistry

According to the procedure shown in Tables 3-1 and 3-2, immunostaining was performed at the pre-formation and post-formation stages for endodermal, mesodermal, and ectodermal cell markers, and ECM molecules: mucosal epithelial cells (caudal type homeobox 2, Cdx2; E-cadherin), pan-mesenchymal cells (vimentin), smooth muscle cells/myofibroblasts (alpha-smooth muscle actin,

α SMA), lymphatic endothelial cells (lymphatic vessel endothelial hyaluronan receptor 1, LYVE-1), vascular endothelial cells (CD31 antigen, CD31; CD34 antigen, CD34), neural crest cells (SRY [sex determining region Y]-box 10, Sox10), neurons (tubulin, beta 3 class III, Tuj1), fibronectin, collagen I, pan-tenascin, collagen IV, pan-laminin, and laminin 1/2. In this study, “pan-tenascin” indicates all members of the tenascin family (tenascin C/R/W/X), “pan-laminin” indicates all laminin isoforms, and “laminin 1, 2” indicates laminin 1 (α 1, β 1, γ 1) and 2 (α 2, β 1, γ 1) isoforms. Details of the procedures are described in Chapter 2.

Whole-mount Immunohistochemistry for Tuj1

For Tuj1, whole-mount immunohistochemistry was performed at the post-formation stage. Whole embryos fixed with 4% PFA were treated with 6% H₂O₂/methanol for whitening and dehydration. After treatment with dimethyl sulfoxide/methanol/10% Triton X-100 for 30 minutes, the embryos were treated with blocking buffer (5.0 mM Tris, 0.9% NaCl, 0.1% Triton X-100, 5.0% skim milk, pH 7.8) for 6 hours and incubated with primary antibody/blocking buffer for 2 days. After washing in buffer (5.0 mM Tris, 0.9% NaCl, 0.1% Triton X-100, pH 7.8), the embryos were treated with secondary antibody/blocking buffer. Finally, the embryos were incubated with DAB-H₂O₂ and post-fixed with 10% neutral-buffered formalin.

Alcian Blue Staining for Proteoglycan Detection

Cross- and sagittal-sections were deparaffinized and stained with pH1.0 and pH2.5 Alcian Blue. Alcian Blue staining at pH1.0 detects proteoglycans containing sulfate groups, while that at pH2.5 detects proteoglycans primarily containing carboxyl groups, along with sulfate groups. Briefly, following incubation with either 1N HCl (pH1.0) or 3% acetic acid (pH2.5) for 3 min, the sections were treated with 1% Alcian Blue reagent (either pH1.0 or pH2.5). Next, the sections were washed with either 100% ethanol (pH1.0) or 3% acetic acid (pH2.5) for 5 min. To confirm the identity of the Alcian Blue stained area, the author counterstained selected sections with eosin at the post-formation stage, after Alcian Blue staining, by treating the sections with eosin reagent for 1 sec (pH 1.0) or 10 sec (pH2.5).

Immunofluorescence for N-cadherin

DJF sections at the pre-formation and the post-formation stage (semi-serial, 3- μ m-thick) were deparaffinized and heated with citrate buffer, pH6.0. After blocking, the sections were treated with primary antibodies against N-cadherin, and then with Alexa Fluor 546-labeled secondary antibodies (Life technologies, Waltham, MA, USA).

Image Processing for Histoplanimetry

In this study, the author measured the integrated density (IntDen) of stained-positive reactions and the immunopositive cell density in the measured areas between the inner and outer bending sides on the histochemical stained sections of

the DJF using ImageJ (Fig. 3-1). For the measurement of the IntDen, IntDen refers to the sum of signal intensities over a defined area. Because the signal was not immediately clear, digital images were processed as follows. The author drew boundaries between the inner and outer bending sides of the DJF on digital images (Fig. 3-1). At the pre-formation stage, the author respectively defined the inner and outer areas as the left and right areas of the DJF mesenchyme, not including the mucosal epithelium, divided by a straight line crossing the dorsal and ventral mesenteries (Fig. 3-1a). At the post-formation stage, the author placed a 100 μm , or 25 μm for the analysis of the mucosal epithelium, square area around the center of the top of the DJF and defined the boundary between the inner and outer bending sides of the DJF as the mucosal epithelium (Fig. 3-1b). In order to highlight the signal, the author reduced the background color by using Photoshop (Adobe Systems Incorporated; San Jose, CA, USA). After that, the author converted RGB color images into black and white, and subsequently switched the signal color from black to white. Finally, the author analyzed IntDen for the signal on the processed images using ImageJ. For the measurement of the immunopositive cell density, the measured area was the same as the measurement of the IntDen (Fig. 3-1).

Histoplanimetry for the Mucosal Epithelial Cells

The immunohistochemical sections of the mucosal epithelial cell markers were used for histoplanimetry (Fig. 3-1). At the pre-formation stage, straight lines crossing the dorsal and ventral mesenteries were drawn on digital images (Fig. 3-

1a), and the Cdx2-positive cell density (number/ μm^2) and IntDen of E-cadherin-positivity were measured using ImageJ. These values were compared between the inner and outer bending sides of the mucosal epithelium in the DJF.

At the post-formation stage, one sagittal-section from each of more than four dissected gut tubes was histoplanimetrically analyzed after the immunohistochemical assay for Cdx2 and E-cadherin. The Cdx2-positive cell density and IntDen of E-cadherin-positivity were measured with ImageJ, and the averages of the inner and outer bending sides of the DJF were compared. In particular, the analyzed area for the mucosal epithelium was the inner or outer mucosal epithelium that was located in the range of 25 μm from the center of the top of the DJF (Fig. 3-1b).

Histoplanimetry for Cells in the Mesenchymal Area

For the analysis of cell population and differentiation of cells in the mesenchymal area, immunohistochemical sections assayed for mesodermal or ectodermal cell markers were used for histoplanimetry (Fig. 3-1). The IntDen of vimentin- or CD31- and CD34-positivity and the number of Sox10- or Tuj1-positive cells were quantified using ImageJ, and the latter was expressed as the positive cell density (number/ μm^2). At the pre-formation and post-formation stages, the analyzed area was defined as described above (Fig. 3-1). The average of three sections from each specimen was used as an individual value, and the average of the positive cell density or IntDen of more than four specimens was compared between the inner

and outer bending sides of the DJF. For Sox10 and Tuj1, the positive cell density in the inner and outer bending sides of the DJF was also compared between the corresponding sides of the straight parts of the midgut adjacent to the DJF, as a comparative control.

Histoplanimetry for ECM Distribution

For analysis of ECM distribution in the mesenchymal area, Alcian Blue-stained and immunohistochemical sections were used for histoplanimetry (Fig. 3-1). The IntDens of Alcian Blue- and immuno-positivity were quantified using ImageJ. To easily detect the differences between the inner and outer bending sides, the author calculated their respective IntDen ratios in the following manner: the IntDen of the inner side divided by itself (IntDen ratio of the inner side); the IntDen of the outer side divided by the IntDen of the inner side (IntDen ratio of the outer side). Therefore, the value of the IntDen ratio of the inner side was always equal to 1.0, and the author could easily calculate the differences as the relative changes in the value of the outer side.

For analyses at both stages, the average IntDen of three sections from each embryo was considered an individual value, which was used for calculating the individual IntDen ratio as described above. The average of the IntDen ratios for more than four specimens was compared between the inner and outer bending sides of the DJF.

For the ECM molecules located at the epithelial basement membrane

(collagen IV, pan-laminin, laminin 1/2); in particular, the IntDen ratios for immunopositive reactions were measured separately on the outside and inside areas. Briefly, the author defined the boundary between the two areas as the line drawn 25 μm below the surface of the DJF at the pre-formation and post-formation stages (Fig. 3-1). Therefore, the outside area included both the mesothelial and endothelial basement membranes beneath the mesothelium, while the inside area included the mucosal epithelial and endothelial basement membrane.

Statistical Analysis

Results were statistically analyzed as described in Chapter 2.

Results

Cell Population and Differentiation of the Mucosal Epithelium in the Developing Mouse DJF

At the both pre-formation and post-formation stages, immunopositive reactions for the mucosal epithelial cell markers, Cdx2 and E-cadherin, were detected in the nucleus (Figs. 3-2a and b) and the cytoplasm or intercellular portion (Figs. 3-2d and e) of the mucosal epithelium in the DJF, respectively. The number of Cdx2-positive cells and the IntDen of E-cadherin-positivity were similar between the inner and outer bending sides of the mucosal epithelium in the DJF at both stages (Figs. 3-2a, b, d and e), and these observations were confirmed by histoplanimetry (Figs. 3-2c and f).

Cell Population and Differentiation in the Mesenchymal Area of the Developing Mouse DJF

To evaluate the population and differentiation of cells derived from the mesoderm, the expression of vimentin (pan-mesenchymal cells), α SMA (smooth muscle cells, myofibroblasts), LYVE-1 (lymphatic endothelial cells), CD31 and CD34 (vascular endothelial cells) proteins were evaluated at the pre-formation and post-formation stages by immunohistochemistry (Figs. 3-3 and 3-4).

Vimentin-positivity was detected in the cytoplasm of almost all cells in the mesenchymal area at both stages, including vascular endothelial cells (Figs. 3-3a and b). At the post-formation stage, vimentin-positive cells had well-developed

cytoplasmic processes, and the longitudinal axes of these cells were arranged along the inner-outer bending axis in the inner side, but along the perpendicular direction to the axis in the outer side (Fig. 3-3b). On the other hand, no α SMA-positive reaction was detected in both stages (Figs. 3-3d and e). In histoplanimetry, the IntDen of vimentin-positivity was significantly higher in the inner side than in the outer side at the post-formation stage (Fig. 3-3c).

LYVE-1-positive lymph vessels were rarely observed in the mesenchymal area of the DJF at the pre-formation and post-formation stages (Figs. 3-4a and b). Interestingly, some endothelial cells of blood vessels in the mesenchymal area displayed LYVE-1-positivity, as shown in Fig. 3-4a. CD34-positivity was mainly detected in the endothelial cells of blood vessels and in the scattered cells comprising the mesenchymal area, and the latter indicated capillary vessels (Figs. 3-4c and d). The IntDen of CD34-positivity did not show any significant difference at the pre-formation and post-formation stages (Fig. 3-4e). On the other hand, CD31-positivity was also detected in the endothelial cells of blood vessels (Fig. 3-4f). However, the IntDen of CD31-positivity showed higher in the inner side than in the outer side of the DJF at the post-formation stage (Fig. 3-4g).

Next, immunohistochemical assays for Sox10, neural crest cells, and Tuj1, differentiated neurons, were performed at the pre-formation and post-formation stages (Fig. 3-5). Sox10-positivity was detected in the nuclei of cells scattered in the middle layer of the mesenchymal area at both stages (Figs. 3-5a and b). Tuj1-positivity was observed in the cytoplasm of cells in the middle layer of the

mesenchymal area, which is the same localization as that of the Sox10-positive cells, at both stages (Figs. 3-5d and e). Interestingly, Tuj1-positive cells were more abundantly observed in the inner side compared to the outer side, and the size of Tuj1-positive cells tended to be larger in the inner side than in the outer side (Figs. 3-5d and e). These asymmetric populations of Tuj1-positive cells were also confirmed in the whole-mount immunohistochemistry analysis (Figs. 3-5g–i), and the reticular Tuj1-positive cells were abundantly observed in the inner side at the post-formation stage (Fig. 3-5h). To evaluate the populations of Sox10- and Tuj1-positive cells, the density of immunopositive cells was compared histoplanimetrically between the inner and outer bending sides of the DJF (Figs. 3-5c and f). The density of Tuj1-positive cells was higher in the inner side than in the outer side at the pre-formation and post-formation stages (Fig. 3-5f), while no significant difference was detected in the density of Sox10-positive cells at both stages (Fig. 3-5c) and in any parameters in the straight midgut part used as a control (Figs. 3-5c and f).

Distribution of Proteoglycans in the Developing Mouse DJF

In order to detect proteoglycans containing sulfate and carboxyl groups, Alcian Blue staining at pH1.0 and pH2.5, respectively, was performed at the pre-formation and post-formation stage DJFs (Fig. 3-6). In the gut tube, Alcian Blue-positivity at both pH values was detected around the cells in the mesenchymal area, but not within their cytoplasm or nuclei (Figs. 3-6a–c). Alcian Blue-positivity at pH1.0 was

detected mainly in the intercellular spaces as well as epithelial basement membrane of the mesenchymal area at both stages (Figs. 3-6a–c; daggers, arrowheads, and arrows). Meanwhile, Alcian Blue-positivity at pH2.5 was detected only in the intercellular spaces of the mesenchymal area at both stages (Figs. 3-6e–g; daggers, and arrowheads). At the pre-formation stage, the IntDen ratios of positive reactions were higher at the outer side of the DJF than at the inner side, for both pH1.0 (Fig. 3-6d) and pH2.5 (Fig. 3-6h); a significant difference was observed for the latter. However, the IntDen ratios for both stain-positive reactions were significantly higher at the inner side of the DJF than at the outer side at the post-formation stage (Figs. 3-6d and h).

Distribution of Fibronectin and Collagen I in the Developing Mouse DJF

To detect other ECM molecules, immunohistochemistry was performed at the pre-formation and post-formation stage DJFs (Figs. 3-7, 3-8, 3-9 and 3-10).

At both stages, fibronectin-positivity was detected at the intercellular spaces of the whole-mesenchymal area and the mucosal epithelial basement membrane (Figs. 3-7a and b; daggers, and arrows). The IntDen ratio for fibronectin-positivity was significantly higher at the inner side of the DJF than at the outer side at the post-formation, but not pre-formation stage (Fig. 3-7c).

Collagen I-positivity was detected in part of the intercellular spaces in the mesenchymal area of the DJF (Figs. 3-7d–g; arrowheads). The reaction intensities were weaker than that for the other ECM molecules examined. At the pre-formation

stage, the reactions were limited to the mesenchymal area, close to the dorsal and ventral mesenteries (Fig. 3-7d; black arrowheads). Further, the IntDen ratio for collagen I-positivity was not different between the inner and outer bending sides of the DJF (Fig. 3-7h). However, at the post-formation stage, the reactions were much stronger at the outside of the mesenchymal area at the inner side of the DJF (Figs. 3-7e–g). Some reactions appeared to be distributed along a line, similar to the basement membrane (Fig. 3-7g; white arrowheads). The IntDen ratio for collagen I-positivity was significantly higher at the inner side of the DJF than at the outer side at the post-formation stage (Fig. 3-7h).

Distribution of Pan-tenascin in the Developing Mouse DJF

At the pre-formation stage, pan-tenascin-positivity was broadly detected at the intercellular spaces from the mesothelial to the mucosal epithelial basement membranes in the inner side of the DJF (Figs. 3-8a–c). In particular, the reactions at the intercellular spaces close to the mesothelial basement membrane (Fig. 3-8c) tended to be stronger than those at the intercellular spaces close to the mucosal epithelial basement membrane (Fig. 3-8a; arrowhead). Strong positive reactions were also detected at the dorsal mesentery (Fig. 3-8a; DM). The IntDen ratio for pan-tenascin-positivity was significantly higher at the inner side of the DJF than at the outer side at the pre-formation stage (Fig. 3-8e). However, at the post-formation stage, it was only faintly detected at the intercellular spaces of the outside mesenchymal area at the inner and outer bending sides of the DJF (Fig. 3-8d). The

dorsal mesentery, meanwhile, maintained its pan-tenascin-positivity (Fig. 3-8d; arrowheads). Further, the IntDen ratio for pan-tenascin-positivity did not differ between the inner and outer sides of the DJF at the post-formation stage (Fig. 3-8e).

Distribution of Collagen IV in the Developing Mouse DJF

Next, in order to examine the basement membrane, the author used immunohistochemistry to detect collagen IV and laminins (Figs. 3-9 and 3-10). The author independently measured the IntDen ratios at the inside area for the mucosal epithelial and endothelial basement membranes, and at the outside area for the mesothelial and endothelial basement membrane beneath the mesothelium (see Fig. 3-1). Collagen IV-positivity was detected mainly in the mucosal epithelial and endothelial basement membranes at both stages (Figs. 3-9a and d; arrows), partly in the mesothelial basement membrane of the DJF at the pre-formation stage, but rarely at the post-formation stage (Figs. 3-9a–d; arrowheads). At the pre-formation stage, the collagen IV-positivity in the mesothelial basement membrane was stronger and more assembled at the inner, than at the outer side of the DJF (Figs. 3-9b and c). Therefore, the IntDen ratio for collagen IV-positivity in the outside area was significantly higher at the inner side of the DJF than at the outer side; however, that for the inside area did not differ at the pre-formation stage (Fig. 3-9e). On the other hand, at the post-formation stage, the IntDen ratio for the outside area was not significantly different between the inner and outer sides of the DJF, while that for the inside area was significantly higher at the inner, than at the outer side of the

post-formation stage DJF (Fig. 3-9e).

Distribution of Pan-laminin and Laminin 1/2 in the Developing Mouse DJF

Pan-laminin-positivity was detected in the mucosal epithelial, endothelial, (Figs. 3-10a and d; arrows) and mesothelial (Figs. 3-10a–f; arrowheads) basement membranes in the DJF at the pre-formation and post-formation stages. Compared with collagen IV-positivity, the pan-laminin-positive reactions in the mesothelial basement membrane, in particular at the pre-formation stage, was broader and more scattered (Figs. 3-9a–c and 3-10a–c). At the pre-formation stage (Fig. 3-10a), the IntDen ratios for pan-laminin-positivity in both the outside and inside areas were significantly higher at the outer side of the DJF than at the inner side (Figs. 3-10b, c and m). On the other hand, at the post-formation stage (Fig. 3-10d), the IntDen ratios for both the outside and inside areas were significantly higher at the inner side of the DJF than at the outer side (Figs. 3-10e, f and m).

Meanwhile, laminin 1/2-positivity was detected in the mucosal epithelial (Figs. 3-10g and j; arrows) and mesothelial (Figs. 3-10g–l; arrowheads) basement membranes. Additionally, it was either absent or present in low amounts in the endothelial basement membrane, in the DJF at the pre-formation and post-formation stages (Figs. 3-10g and j). At the pre-formation stage, laminin 1/2 positivity in the mesothelial basement membrane appeared as a line, and assembled at the inner side, while being broadly scattered at the outer side (Figs. 3-10h and i). The IntDen ratio for laminin 1/2-positivity in the outside area was significantly higher at the outer

side of the DJF than at the inner side, similar to that for the pan-laminin-positive reactions (Fig. 3-10n). However, at the post-formation stage, laminin 1/2 positivity in the mesothelial basement membrane was weaker and appeared scattered in both the sides (Figs. 3-10k and l). The IntDen ratios for both the outside and inside areas did not differ between the inner and outer sides of the post-formation stage DJF (Fig. 3-10n). This was not similar to the IntDen ratio for the pan-laminin-positive reactions (Figs. 3-10m and n).

Since significant differences were observed for the IntDen ratios for all the basement membrane ECM molecules at the outside area of the pre-formation stage DJF, the author hypothesized that the morphological property of the cell in the outside area differs from that in the inside area. To test this, immunohistochemistry for N-cadherin, an adhesion molecule, was performed at the pre-formation and post-formation stage DJFs (Figs. 3-11). Although N-cadherin-positivity was detected at the most of mesenchymal cells, the results indicated strong N-cadherin-positivity in several cells surrounding the mucosal epithelium, which were neural crest cells and neurons as described in our previous study (Fig. 3-11a and d; arrows). In addition, the mesothelium in both the dorsal mesentery and the outside area of the mesenchymal area extending from the dorsal mesentery was N-cadherin-positive (Figs. 3-11a and d). N-cadherin-positivity in the outside area surrounded the mesothelial cells, in particular at the inner side, while that at the outer side was weak at the pre-formation stage (Figs. 3-11b and c; arrowheads). On the other hand, the author did not detect clear difference beneath the mesothelium between the inner

and outer bending sides in the post-formation stage DJF, stained with N-cadherin antibodies (Figs. 3-11e and f).

Discussion

In this study, the author demonstrated asymmetric distributions of several gut component cells and ECM molecules during mouse DJF formation, as summarized in Table 3-3.

The mucosal epithelial cell marker Cdx2 is involved in gut morphogenesis as a transcriptional factor (Grainger et al. 2010). E-cadherin is also implicated in epithelial cell adhesion and signal transduction and is also required for gut epithelium formation (Bondow et al. 2012). However, in this study, no asymmetry was observed in the histoplanimetric scores of the Cdx2- and E-cadherin-positivity in the mucosal epithelium of the DJF at any stage. For the immunohistochemical analysis of the cells in the mesenchymal area of the DJF, the IntDen of vimentin-positivity was significantly higher in the inner side than in the outer side of the DJF at the post-formation stage. Vimentin, a marker of pan-mesenchymal cells, was expressed in almost all mesenchymal cells of the DJF at both the pre-formation and post-formation stages. Although the differentiation of mesenchymal cells to smooth muscle cells occurs from E11.0 to E13.0 in the developing gut tubes of mice (Tondeleir et al. 2009), the expression of α SMA was not detected in the DJF at any stage. Therefore, the differentiation of smooth muscle cells in the DJF might start after DJF formation. In Chapter 2, the author clarified that the mesenchymal cells were more crowded in the inner side compared with the outer side of the DJF. Taken together, these data suggest that the asymmetric density of mesenchymal cells, not their asymmetric differentiation, is a morphological characteristic of the developing

mouse DJF.

Both CD31 and CD34 are markers of vascular endothelial cells. In this study, the IntDens of CD31- and CD34-positivity were observed in the mesenchymal area of the DJF. Interestingly, there was no asymmetric difference in the IntDen of CD34-positivity between the inner and outer sides of the DJF, while the IntDen for CD31-positivity was significantly higher at the inner side, than at the outer side at the post-formation stage. The section stained by CD34 antibodies showed considerable background staining because of CD34 expression in other cells including vascular endothelial progenitor cells, embryonic fibroblasts, and multipotent mesenchymal stromal cells (Sidney et al. 2014). The vessels stained more weakly than did the section stained by CD31 (See Figs. 3-4d and f). This affected the differences between the IntDen for the CD34- and CD31-positive reactions. The author assumes that the asymmetric IntDen of CD31-positivity also suggests the asymmetric density of blood vessels between the inner and outer bending sides of the DJF, corresponding with that of mesenchymal cells.

On the other hand, the expression of LYVE-1, a marker of lymphatic endothelial cells, was also observed and overlapped with the expressions of blood vessel markers, and the vessels that expressed both LYVE-1 and CD34 contained several red blood cells. Lymphatic vessel development was reported to start from approximately E13.0 in the gastrointestinal tract (Kim et al. 2007). Therefore, in this study, the author assumes that LYVE-1-positive reactions in the DJF might be non-specific or that there might be some common antigens recognized by the anti-

LYVE-1 antibody in the embryonic blood vessels.

In striking contrast, Tuj1-positive differentiated neurons were more abundant in the inner side of the DJF than in the outer side. This result indicates two putative asymmetries: (1) in the differentiation of neurons, or (2) in the migration of undifferentiated neurons, i.e., neural crest cells. Neural crest cells migrate from the vagal neural crest into the foregut at about E9.5 in mice. These cells migrate cranio-caudally, proliferate, and differentiate first into neurons as early as E10.5 and later into glia (Harrison and Shepherd 2013; Lake and Heuckeroth 2013). This migration is complete by E14.0 in mice (Lake and Heuckeroth 2013). The wavefront of migrating neural crest cells passes the DJF at around E10.5, the pre-formation stage in the DJF, and reaches the cecum at around E11.5, the post-formation stage in the DJF (Lake and Heuckeroth 2013). In this study, no difference was observed in the population of Sox10-positive cells; Sox10 is a marker of neural crest cells. This means that neural crest cells migrated at the same rate in both sides of the DJF, but that neural differentiation occurred earlier in the inner side of the DJF than in the outer side. In fact, the Tuj1-positive cells in the inner side were larger than those of the outer side of the DJF.

Remarkably, the mechanism under the increasing number of Tuj1-positive cells in the inner side of the DJF seemed to be different from that under the increasing densities of Vimentin- and CD31-positivity. For the increasing Vimentin- and CD31-positivity in the inner side of the DJF, the author suggests that the accumulation of mesenchymal cells in the inner side of the DJF is one of the reason

and that this accumulation is related to the asymmetric elongation between the inner and outer bending sides of the DJF. On the other hand, Tuj1-positive cells did not seem to be affected by the accumulation because the asymmetric distribution is observed even at the pre-formation stage. Therefore, the author suggests that several signaling pathways including BMP, hedgehog, and retinoid (Harrison and Shepherd 2013; Lake and Heuckeroth 2013; Liu and Ngan 2014), should show different expressions between the inner and outer bending sides of the DJF. Interestingly, enteric nervous system influences on mesenchymal-epithelial interaction crucial for gut morphogenesis. For example, the development of the pancreatic epithelium requires ectoderm derived cells (Nekrep et al. 2008). Moreover, enteric nervous system affects smooth muscle development in the chick stomach (Faure et al. 2015). Therefore, the author supposes that the increasing Tuj1-positive cells in the inner side are related to DJF formation.

In the analyses for ECM molecules, Alcian Blue-positivity at the pre-formation and post-formation stages was stronger at the outer and inner side of the DJF, respectively, than at the opposite side at both pH1.0 and pH2.5. Alcian Blue staining detects proteoglycans, which are made of a core protein containing several types of glycosaminoglycan chains. Glycosaminoglycans are roughly divided into chondroitin sulfate, heparan sulfate, dermatan sulfate, and keratan sulfate. These glycosaminoglycan chains have abundant sulfate groups and carboxyl groups that stain blue with Alcian Blue. Recent studies reported that some heparan sulfate proteoglycans, such as syndecan, control the localization of several growth factors

and modify their activities and reception in mammals (Hynes 2009; Shimokawa et al. 2011; Iozzo and Schaefer 2015). However, the author reported the higher cell proliferation rate in the outer side of the DJF than in the inner at the post-formation, but not pre-formation stage in Chapter 2. There are many kinds of proteoglycans, which play different roles, even within the heparan sulfate proteoglycan group. For example, perlecan is known as a regulator of angiogenesis (Iozzo and Schaefer 2015). Unfortunately, investigating each proteoglycan component with Alcian Blue was beyond the scope of this study. However, the author demonstrated that the distribution of proteoglycans alters during DJF formation.

The IntDen ratios of fibronectin- and collagen I-positivity were higher at the inner side of the DJF than at the outer side at the post-formation stage, suggesting the abundance of these ECM molecules. Fibronectin is a large glycoprotein ubiquitously expressed throughout the body. An important property of fibronectin is its ability to bind to other ECM molecules and to integrin receptors on the cell surface (Labat-Robert 2012). On the other hand, collagen I is a fibril-forming collagen that is abundantly expressed in interstitial tissues including bones, tendon, ligaments, and dermis. Collagen I provides structural stiffness for the tissue and helps it to resist tensile and torsional stresses (Gelse et al. 2003). In addition, collagen I is also recognized by integrins (Leitinger 2011), which are components of focal adhesion for cell-ECM interactions. Integrins sense mechanical force originating from the ECM and mediate several intracellular signals to control the actin cytoskeleton for cell morphology and migration (Geiger et al. 2009; Janoštiak

et al. 2014). Recent studies have indicated that ECM rigidity is sensed by integrins to guide cell migration toward stiff ECM (Plotnikov et al. 2012). Since the author detected more abundant distribution of fibronectin and collagen I at the inner side of the DJF than at the outer side, the author hypothesized that the inner side had comparatively stiffer ECM. In addition, the author reported that the gut wall of the inner side was thicker than that of the outer side of the DJF, suggesting more abundant cells at the inner side as shown in Chapter 2. Therefore, fibronectin and collagen I at the inner side might contribute to the accumulation of mesenchymal cells, leading to different elongation rates between the inner and outer sides for DJF formation.

The pan-tenascin-positive reactions were higher at the inner side of the DJF than at the outer at the pre-formation stage. The tenascin family includes 4 members: tenascin C, R, W, and X. These proteins are well known for their ability to modulate cell adhesion and migration (Chiquet-Ehrismann and Tucker 2011). Tenascin C is the most studied member because of its spatiotemporal expression during embryogenesis. Recent reports suggest that tenascin C performs several functions including cell proliferation, apoptosis, and differentiation in addition to controlling cell migration (Jones and Jones 2000). Therefore, the author proposed that pan-tenascin affects mesenchymal cells in the DJF because of its ability to modulate cell migration. Notably, the effect of tenascins, in particular tenascin C, depends on the cell type, species, and context (Jones and Jones 2000; Breau et al. 2009; Akbareian et al. 2013). Therefore, the author hypothesized that tenascin C

expression at the inner side of the DJF at the pre-formation stage is necessary for accumulation of mesenchymal cells in the same, through the control of cell migration.

Immuno-positivity for collagen IV, pan-laminin, and laminin 1/2, ECM molecules that make up the epithelial basement membranes, was also detected. Collagen IV is a member of the collagen family and expressed only in the basement membranes. It is a heterotrimer composed of a combination of six α -chains: $\alpha 1\alpha 1\alpha 2$, $\alpha 3\alpha 4\alpha 5$, and $\alpha 5\alpha 5\alpha 6$ (Khoshnoodi et al. 2008). Laminins are also chief components of the epithelial basement membrane, and are heterotrimeric proteins composed of α , β , and γ chains. Since each chain has multiple variants, laminins are divided into more than fifteen isoforms depending on the combination of the three chains (Hohenester and Yurchenco 2013). This study revealed remarkable differences in the IntDen ratios between the inner and outer bending sides of the DJF in the basement membranes located in the outside area, including mainly the mesothelial basement membrane. Interestingly, at the pre-formation stage, the IntDen ratios for collagen IV- and laminins-positivity showed opposite results, suggesting that the components of the basement membrane are different between the inner and outer bending sides of the pre-formation stage DJF. In addition, the IntDen ratio for laminin 1/2-positivity at the pre-formation stage was similar to that of the pan-laminin-positive reactions. Therefore, the difference in pan-laminin-positivity in the outside area is partially caused by the difference in the distribution of laminin 1 or laminin 2. Laminin 1 starts to be expressed in the mucosal epithelial basement

membrane in the early stages of the developing rat intestine, while laminin 2 is expressed around birth (Simon-Assmann et al. 1998). Therefore, the author suggests that the laminin isotype that the laminin 1/2 antibody detected in this study was laminin 1. Interestingly, the study in Chapter 2 showed that cell size in the outside area was significantly different between the inner and outer bending sides of the DJF. Based on this, the author considered the possibility of a difference in cell polarity between the two sides.

Further, this study revealed differences in the adhesive property, as indicated by N-cadherin expression, in cells in the outside area. During gut morphogenesis, laminin 1 is important for the polarization of epithelial cells as well as for cell differentiation (De Alcangelis et al. 1996). Collagen IV is important for basement membrane stability (Pöschl et al. 2003), though there are only few reports on the involvement of collagen IV in morphogenesis. Therefore, the author proposed that the difference in collagen IV-positivity is related to cell morphology, including polarization, and properties of the outside cells at the pre-formation stage.

On the other hand, at the post-formation stage, the IntDen ratio for pan-laminin was higher at the inner side of the DJF than at the outer side, which was not similar to that for the laminin 1/2-positive reactions. The author also proposed that the laminin isoforms abundantly expressed at the inner side at the post-formation stage are different from laminin 1 and 2, suggesting that the components of the basement membrane changed during DJF formation. This was supported by the observation that laminin 1/2-positivity in the outside area decreased at the post-

formation stage. In addition, in the inside area of the post-formation stage DJF, the IntDen ratios for collagen IV- and pan-laminin-positivity were higher at the inner side, than at the outer side. The author hypothesized that this difference was due to the difference in vascular distribution as described above.

For the basement membrane comprising ECM, the components located in the outside area were different at the inner and outer bending sides of the DJF, at least at the pre-formation stage, and changed during DJF formation. The author also showed significant differences in cell morphology in the outside area at the pre- and post-formation stages in Chapter 2. Therefore, a change in composition of the basement membrane located in the outside area might be associated with outside cell morphology.

Although the author detected distinct patterns of ECM distribution, further studies are needed to identify the factors that form these patterns. The author assumes that asymmetric synthesis or degradation of ECM molecules determine the patterns of ECM distribution. Recently, factors contributing to ECM metabolism have been slowly uncovered. TGF- β , a ubiquitous cytokine produced by every cell, promotes ECM secretion through its type II receptor. In an adult mouse gut, the type II receptor is expressed on smooth muscle cells, fibroblasts, and myofibroblasts. In addition, the population of the fibroblasts and myofibroblasts increase during inflammation, and these cells secrete collagen I, collagen IV, and laminin (Whiting et al. 2003). Therefore, TGF- β may be one of the factors that contribute to asymmetric ECM distribution. Moreover, matrix metalloproteinases

(MMPs) are key enzymes for ECM degradation. During chick cardiac looping, ECM asymmetry in the dorsal mesocardium defines the looping direction. This asymmetry appears to be achieved by asymmetric MMP inhibition (Linask et al. 2005). Therefore, MMPs are also candidate factors. In future experiments, the author will identify critical factors for asymmetric ECM distribution.

In conclusion, the distributions of the gut component cells and ECM molecules are different between the inner and outer bending sides of the mouse DJF, and this distribution changes during mouse DJF formation. Those asymmetric distributions might contribute to DJF formation in mice.

Summary

In Chapter 2, the author revealed that asymmetric morphologies between the inner and outer bending sides of the mouse DJF contribute to the asymmetric elongation between the two sides to complete DJF bending. As candidates for the establishment of those asymmetric morphologies, the author focused on the gut component cells and ECM molecules. In this chapter, to elucidate the contribution of the gut component cells and ECM molecules to mouse DJF formation, the author investigated those distributions between the inner and outer bending sides of the developing mouse DJF.

Interestingly, the stain-positive reactions for pan-mesenchymal and blood vessel markers were significantly higher in the inner side of the post-formation stage DJF than in the outer side, corresponding with the mesenchymal cell accumulation in the inner side clarified in Chapter 2. This study also suggested that neural differentiation was earlier in the inner side of the DJF than in the outer side. In addition, all examined ECM molecules showed asymmetric distributions between the inner and outer bending sides during DJF formation, and those distributions shifted through DJF development.

Those asymmetric distributions between the inner and outer bending sides are characteristics of the mouse DJF morphology. At the same time, the author considers that those asymmetric distributions contribute to the establishment of asymmetric morphologies observed in Chapter 2 by controlling the downstream cell signaling of neuron derived molecules and examined ECM molecules in the developing mouse DJF.

Tables and Figures

Table 3-1. Summary of immunostaining conditions for the analysis of the gut component cells

Target	Marker	Primary Antibody	Antigen Retrieval	Second Antibody
Mucosal epithelium	Cdx2	Mouse monoclonal antibodies (BioGenex, Hague, Netherlands)	Target Retrieval Solution, pH9.0 (Dako Japan, Tokyo, Japan)	Simple Stain Mouse MAX-PO(M) (mouse stain kit; Nichirei, Tokyo, Japan)
	E-cadherin	Rabbit polyclonal antibodies (1 : 100; Santa Cruz Biotechnology, Dallas, TX, USA)	Citrate buffer solution, pH6.0	Biotinylated goat anti-rabbit IgG antibodies (SABRO kit; Nichirei)
Pan-mesenchyme	Vimentin	Rabbit monoclonal antibodies (1 : 600; Cell Signaling Technology, Danvers, MA, USA)	Citrate buffer solution, pH6.0	Biotinylated goat anti-rabbit IgG antibodies (SABRO kit; Nichirei)
Smooth muscle	α SMA	Rabbit polyclonal antibodies (1 : 3000; Abcam, Cambridge, UK)	Citrate buffer solution, pH6.0	Biotinylated goat anti-rabbit IgG antibodies (SABRO kit; Nichirei)
Lymphatic endothelium	LYVE-1	Rabbit polyclonal antibodies (1 : 400; AdipoGen, San Diego, CA, USA)	Citrate buffer solution, pH6.0	Biotinylated goat anti-rabbit IgG antibodies (SABRO kit; Nichirei)
Vascular endothelium	CD31	Rabbit polyclonal antibodies (1 : 100; Abcam)	Tris-HCl buffer solution, pH9.0	Biotinylated goat anti-rabbit IgG antibodies (SABRO kit; Nichirei)
	CD34	Rat monoclonal antibodies (1 : 400; Abcam)	Citrate buffer solution, pH6.0	Biotinylated goat anti-rat IgG antibodies (Caltag Medsystems, Buckingham, UK)
Neural crest	Sox10	Goat polyclonal antibodies (1 : 300; Santa Cruz Biotechnology)	Citrate buffer solution, pH6.0	Biotinylated donkey anti-goat IgG antibodies (Santa Cruz Biotechnology)
Neuron	Tuj1	Mouse monoclonal antibodies (1 : 10000 for IHC; 1 : 5000 for WIHC; Abcam)	Citrate buffer solution, pH6.0	Simple Stain Mouse MAX-PO(M) for IHC HRP conjugated goat anti-mouse IgG antibodies (Zymax) for WIHC

α SMA, alpha-smooth muscle actin; Cdx2, caudal type homeobox 2; IHC, immunohistochemistry; LYVE-1, lymphatic vessel endothelial hyaluronan receptor 1; Sox10, SRY (sex determining region Y)-box10; Tuj1, tubulin, beta 3 class III; WIHC, whole-mount immunohistochemistry.

Table 3-2. Summary of immunostaining conditions for the analysis of the extracellular matrix molecules

Target	Primary Antibodies	Antigen Retrieval	Second Antibodies
Collagen I	Rabbit polyclonal antibodies (1 : 1000; Abcam)	Citrate buffer solution, pH6.0	Biotinylated goat anti-rabbit IgG antibodies (SABRO kit; Nichirei)
Collagen IV	Rabbit polyclonal antibodies (1 : 10000; Abcam)	Citrate buffer solution, pH6.0	Biotinylated goat anti-rabbit IgG antibodies (SABRO kit; Nichirei)
Fibronectin	Rabbit polyclonal antibodies (1 : 10000; Abcam)	Citrate buffer solution, pH6.0	Biotinylated goat anti-rabbit IgG antibodies (SABRO kit; Nichirei)
Pan-laminin	Rabbit polyclonal antibodies (1 : 200; Sigma, Saint Louis, MO, USA)	—	Biotinylated goat anti-rabbit IgG antibodies (SABRO kit; Nichirei)
Laminin 1/2	Rabbit polyclonal antibodies (1 : 10000; Novus Biologicals, Littleton, CO, USA)	Citrate buffer solution, pH6.0	Biotinylated goat anti-rabbit IgG antibodies (SABRO kit; Nichirei)
Pan-tenascin	Rat monoclonal antibodies (1 : 10000; Sigma-Aldrich, St. Louis, MO, USA)	Tris-HCl buffer solution, pH9.0	Biotinylated goat anti-rat IgG antibodies
N-cadherin	Rabbit polyclonal antibodies (1 : 2000; Abcam)	Citrate buffer solution, pH6.0	Alexa fluor 546 labeled donkey anti-rabbit IgG antibodies (Life technologies, Waltham, MA, USA)

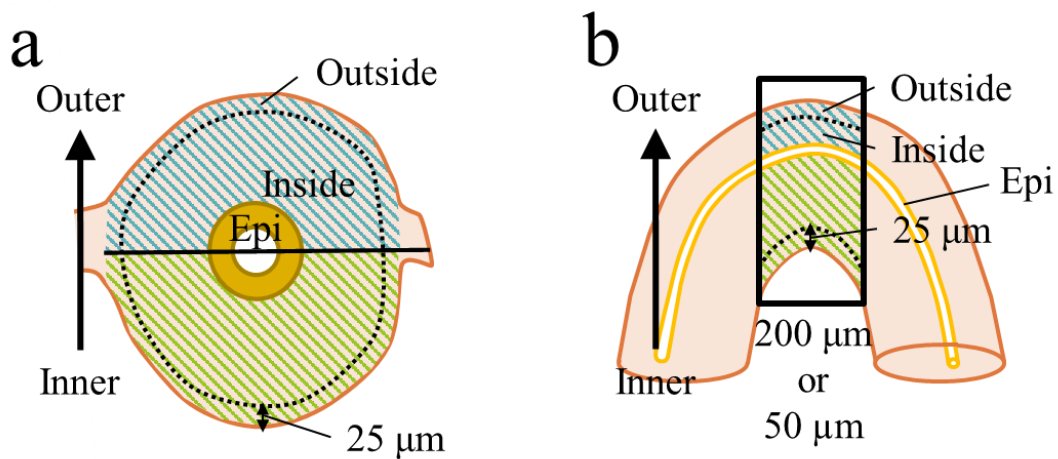


Figure 3-1. Methodologies for the histoplanimetry.

(a) Shema for the histoplanimetry at the pre-formation stage. The boundary between the inner and outer area is defined as the solid line passing on the center of the lumen from the dorsal mesentery to the ventral mesentery. The oblique areas and the mucosal epithelium (Epi) in the inner and outer sides are used for the histoplanimetry of the mesenchymal area and mucosal epithelium, respectively.

(b) Shema for the histoplanimetry at the post-formation stage. The boxes 200 μm and 50 μm wide are the areas for the histoplanimetry of the mesenchymal area and mucosal epithelium, respectively.

The dotted line is a boundary 25 μm beneath the surface of the mesothelium between the outside and inside areas for the analysis of the basement membrane extracellular matrix molecules.

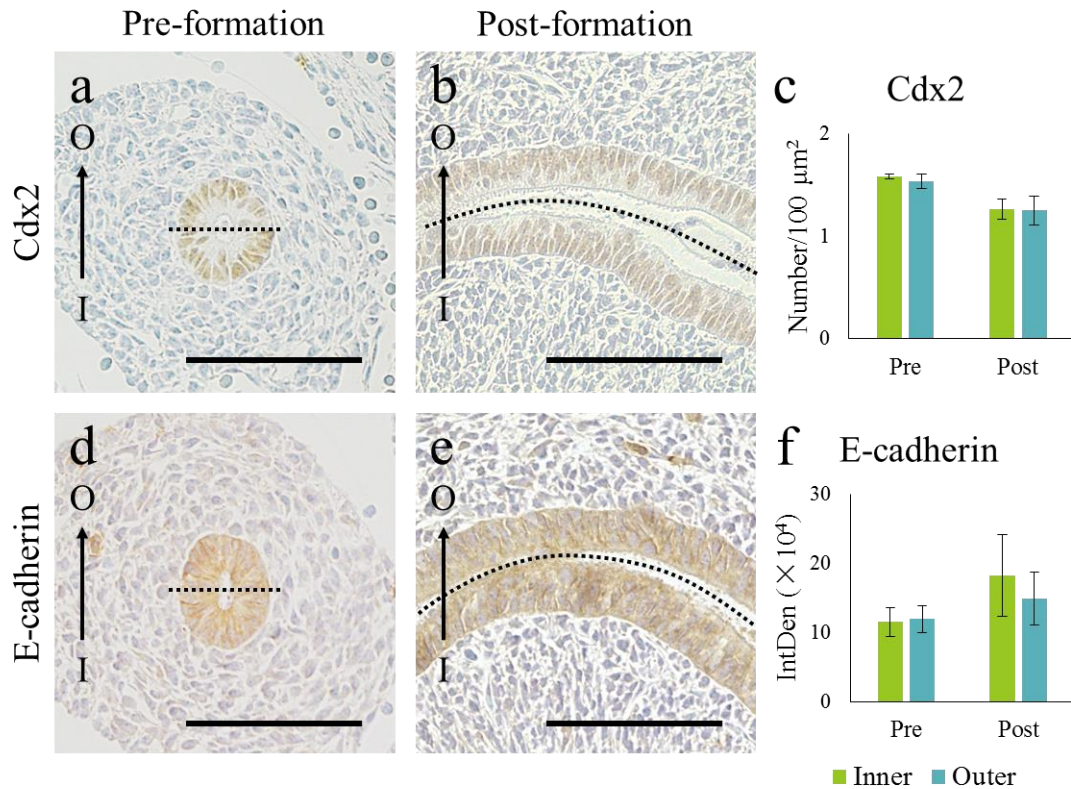


Figure 3-2. Histological features of the mucosal epithelium in the developing mouse duodenojejunal flexure (DJF).

(a and b) Immunohistochemistry for caudal type homeobox 2 (Cdx2) at the pre-formation (a) and the post-formation (b) stage DJFs. Bars, 100 μ m.

(c) Comparison of the density of Cdx2-positive cells in the mucosal epithelium.

(d and e) Immunohistochemistry for E-cadherin at the pre-formation (d) and the post-formation (e) stage DJFs. Bars, 100 μ m; dotted line, boundary between the inner (I) and outer side (O).

(f) Comparison of the integrated density (IntDen) of E-cadherin-positivity in the mucosal epithelium. Values = mean \pm standard error; n = 4.

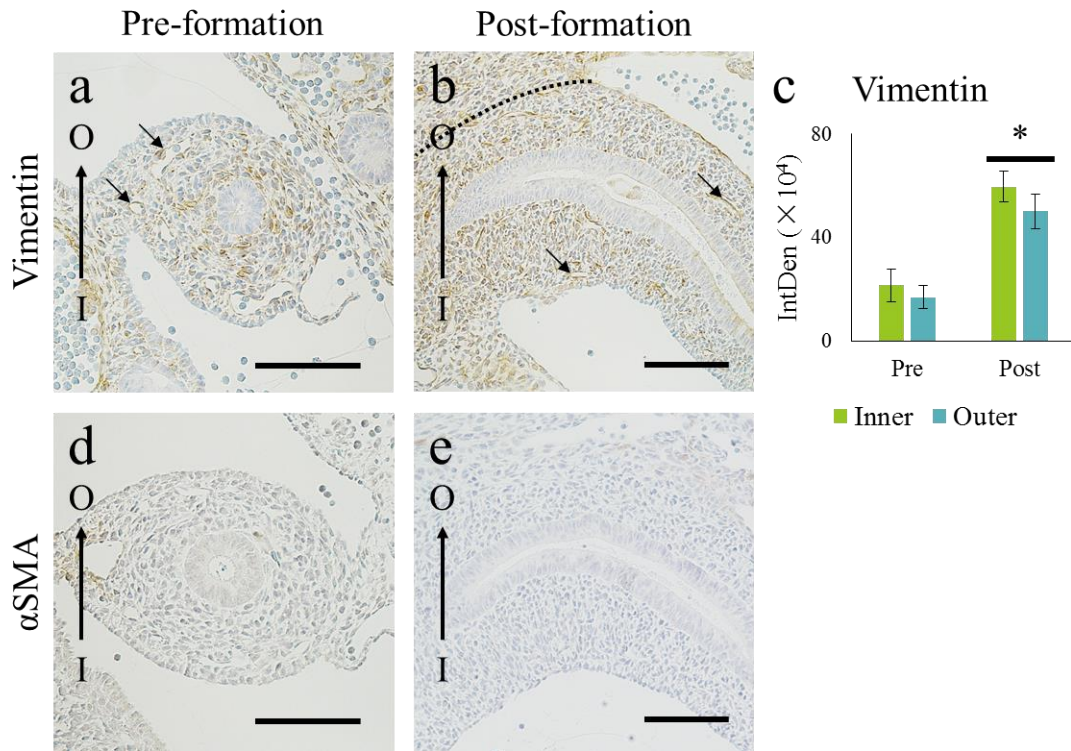


Figure 3-3. Distribution of the pan-mesenchymal and smooth muscle cells in the mesenchymal area of the developing mouse duodenojejunal flexure (DJF).

(a and b) Immunohistochemistry for Vimentin at the pre-formation (a) and the post-formation (b) stage DJFs. Arrows, blood vessels; bars, 100 μm dotted line, boundary between the gut tube and dorsal mesentery.

(c) Comparison of the integrated density (IntDen) of Vimentin-positivity in the mesenchymal area. Values = mean \pm standard error; $n \geq 4$; *, significant difference between the inner and outer side (Wilcoxon test, $P < 0.05$).

(d and e) Immunohistochemistry for alpha-smooth muscle actin (αSMA) at the pre-formation (d) and the post-formation (e) stage DJFs. Bars, 100 μm . I, inner side; O, outer side.

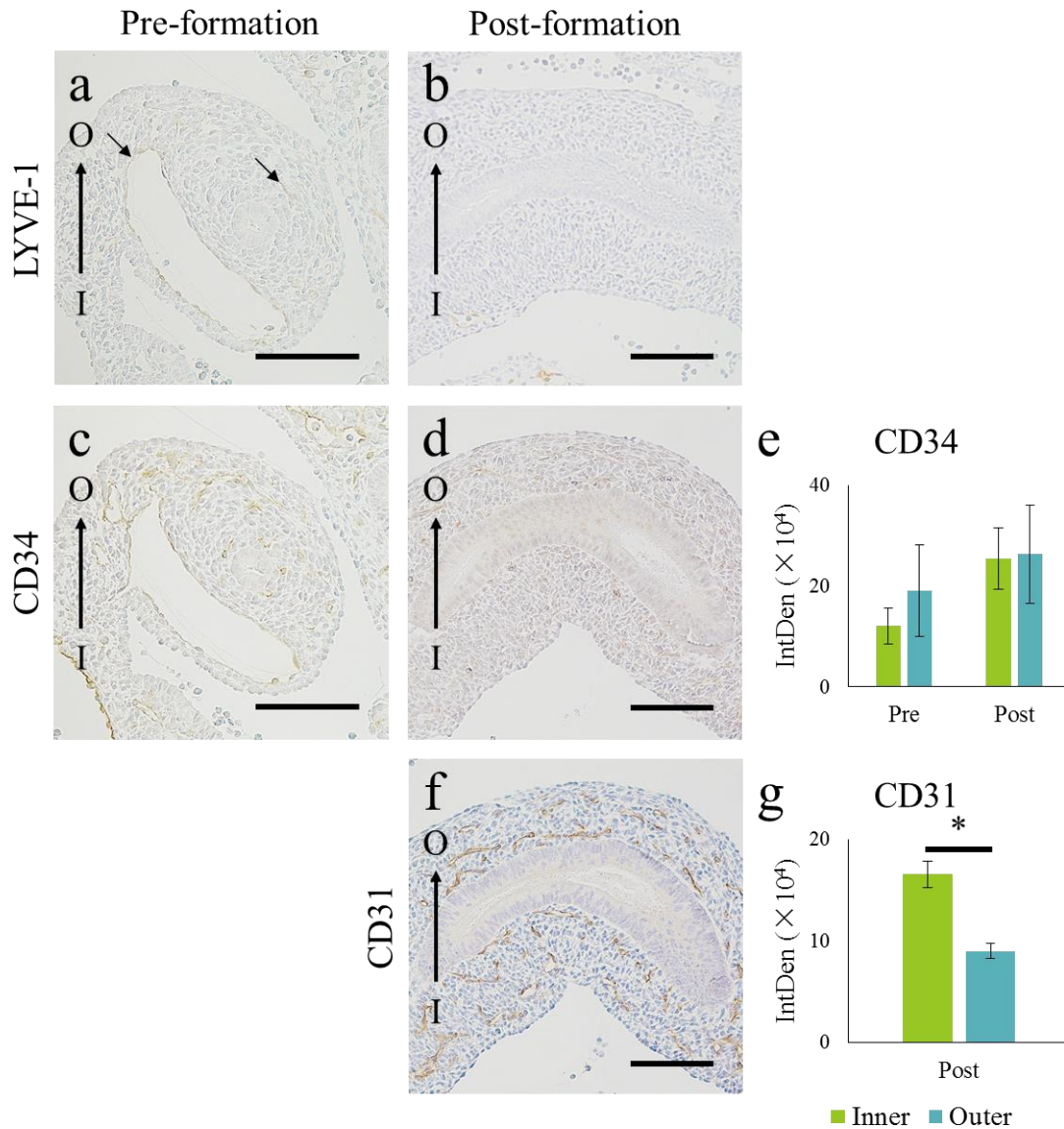


Figure 3-4. Distribution of the lymph and blood vessels in the mesenchymal area of the developing mouse duodenojejunal flexure (DJF).

(a and b) Immunohistochemistry for lymphatic vessel endothelial hyaluronan receptor 1 (LYVE-1) at the pre-formation (a) and the post-formation (b) stage DJFs. Arrows, LYVE-1-positive blood vessels; bars, 100 μm.

(c, d and f) Immunohistochemistry for CD34 antigen (CD34) (c and d) and CD31 antigen (CD31) (f) at the pre-formation (c) and the post-formation (d and f) stage DJFs. Bars, 100 μm; I, inner side; O, outer side.

(e and g) Comparison of the integrated density (IntDen) of CD34- (e) and CD31-positivity (g) in the mesenchymal area. Values = mean ± standard error; $n \geq 4$; *, significant difference between the inner and outer side (Wilcoxon test, $P < 0.05$).

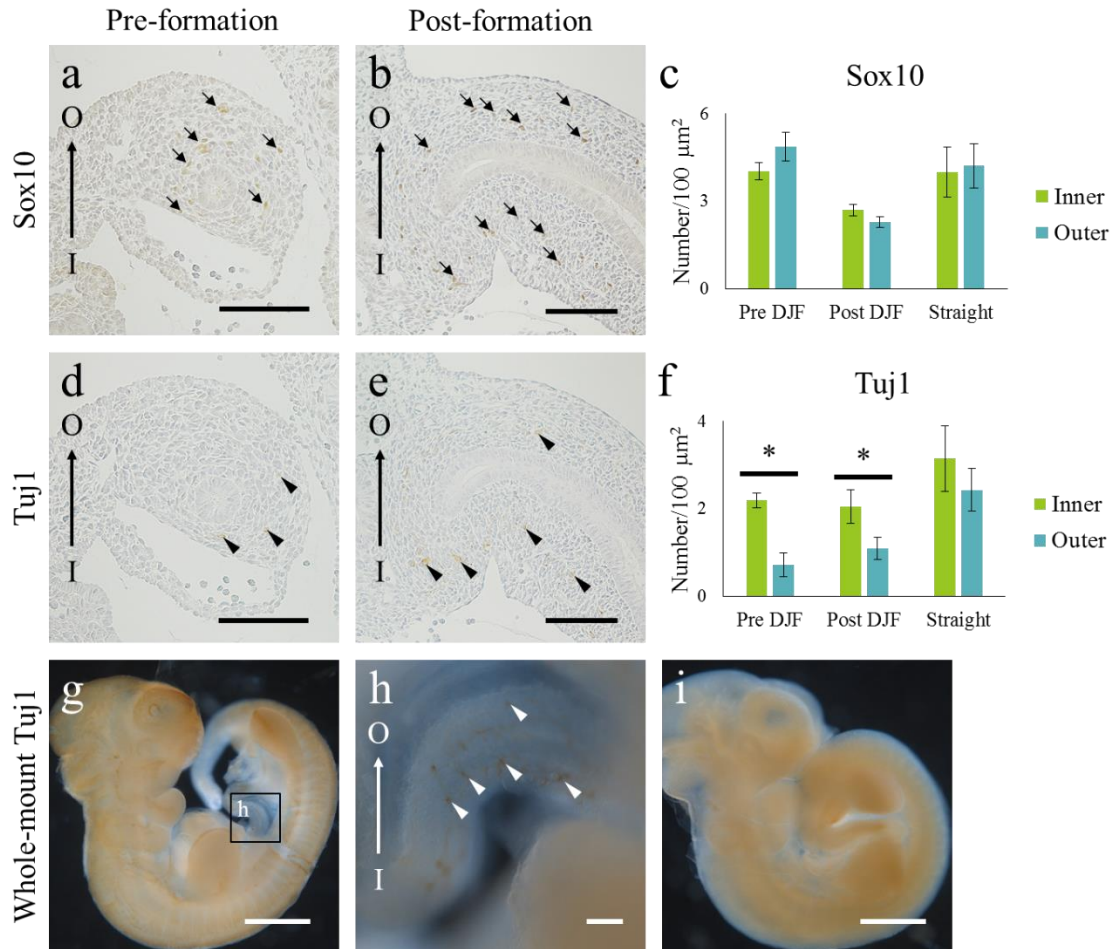


Figure 3-5. Distribution of the exodermal cells in the mesenchymal area of the developing mouse duodenojejunal flexure (DJF).

(a and b) Immunohistochemistry for SRY (sex determining region Y)-box10 (Sox10) at the pre-formation (a) and the post-formation (b) stage DJFs. Arrows, Sox10-positive nuclei; bars, 100 μm .

(c) Comparison of the Sox10-positive nucleus density in the mesenchymal area.

(d and e) Immunohistochemistry for tubulin, beta 3 class III (Tuj1) at the pre-formation (c) and the post-formation (d) stage DJFs. Arrowheads, Tuj1-positive cells; bars, 100 μm .

(f) Comparison of the Tuj1-positive cell density in the mesenchymal area. Values = mean \pm standard error; $n \geq 4$; *, significant difference between the inner and outer side (Wilcoxon test, $P < 0.05$).

(g–i) Whole-mount immunohistochemistry for Tuj1 at the post-formation stage DJF. (i) is a negative control stained by PBST without primary antibodies. Bars, 1 mm (g and i) and 100 μm (h); I, inner side; O, outer side.

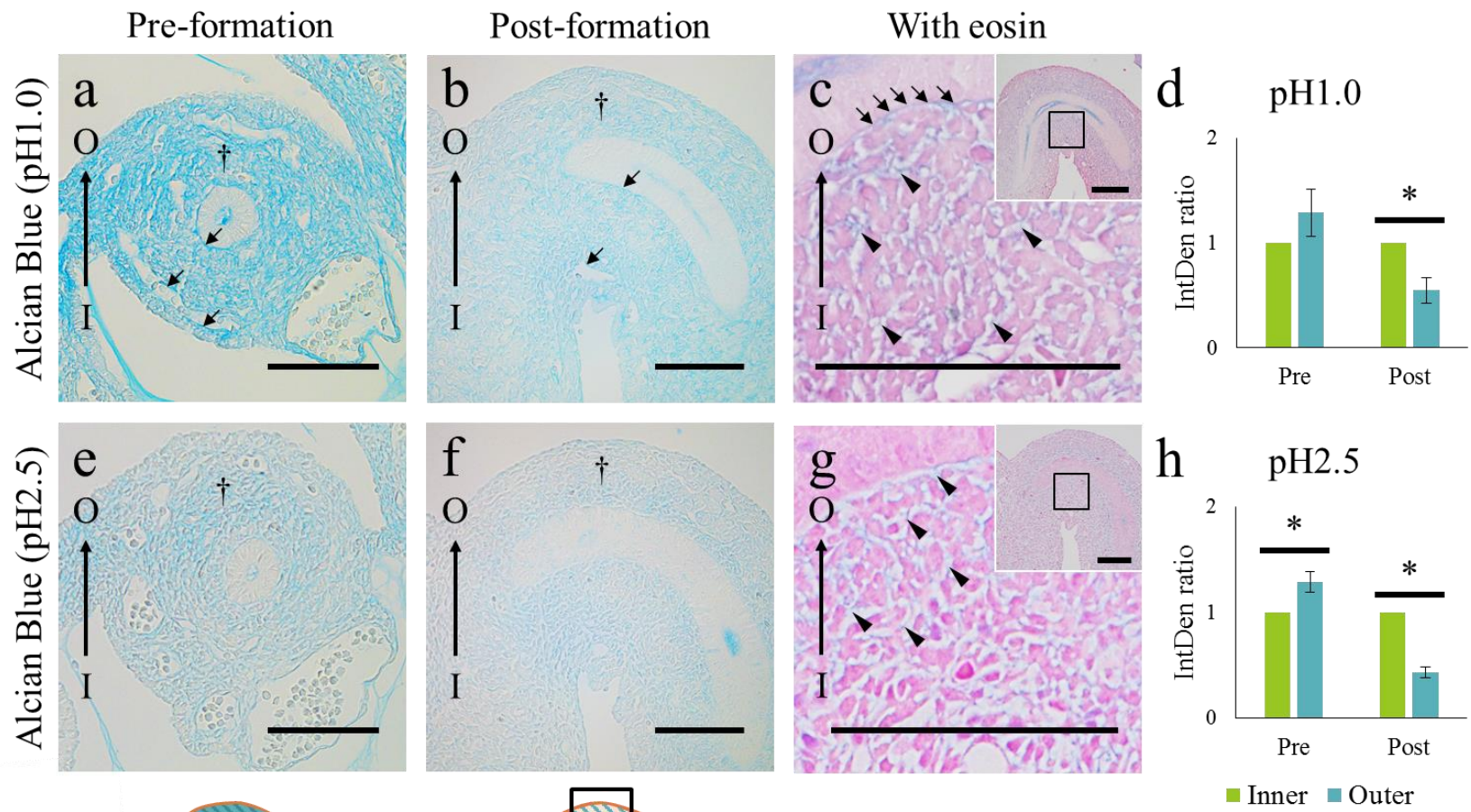


Figure 3-6. Distribution of Alcian Blue-positive proteoglycans in the mesenchymal area of the developing mouse duodenojejunal flexure (DJF).

(a–c) Alcian Blue staining at pH1.0 at the pre-formation (a) and post-formation (b) stage DJFs. (c) is a picture with eosin counterstaining at the post-formation stage and a high magnification view of the inset. Arrows, stain-positive basement membranes; bars, 100 μ m.

d Comparison of the integrated density (IntDen) ratio for the Alcian Blue-positivity at pH1.0.

(e–g) Alcian Blue staining at pH2.5 at the pre-formation (e) and post-formation (f) stage DJFs. (g) is a picture with eosin counterstaining at the post-formation stage and a high magnification view of the inset. Arrowheads and †, stain-positive intercellular space; bars, 100 μ m; I, inner side; O, outer side.

h Comparison of the IntDen ratio for Alcian Blue-positivity at pH2.5. Values = mean \pm standard error; $n \geq 4$; *, significant difference between the inner and outer side (Wilcoxon test, $P < 0.05$).

Schemas beneath the pictures summarize the IntDen ratio difference. Darker blue indicates higher IntDen ratio.

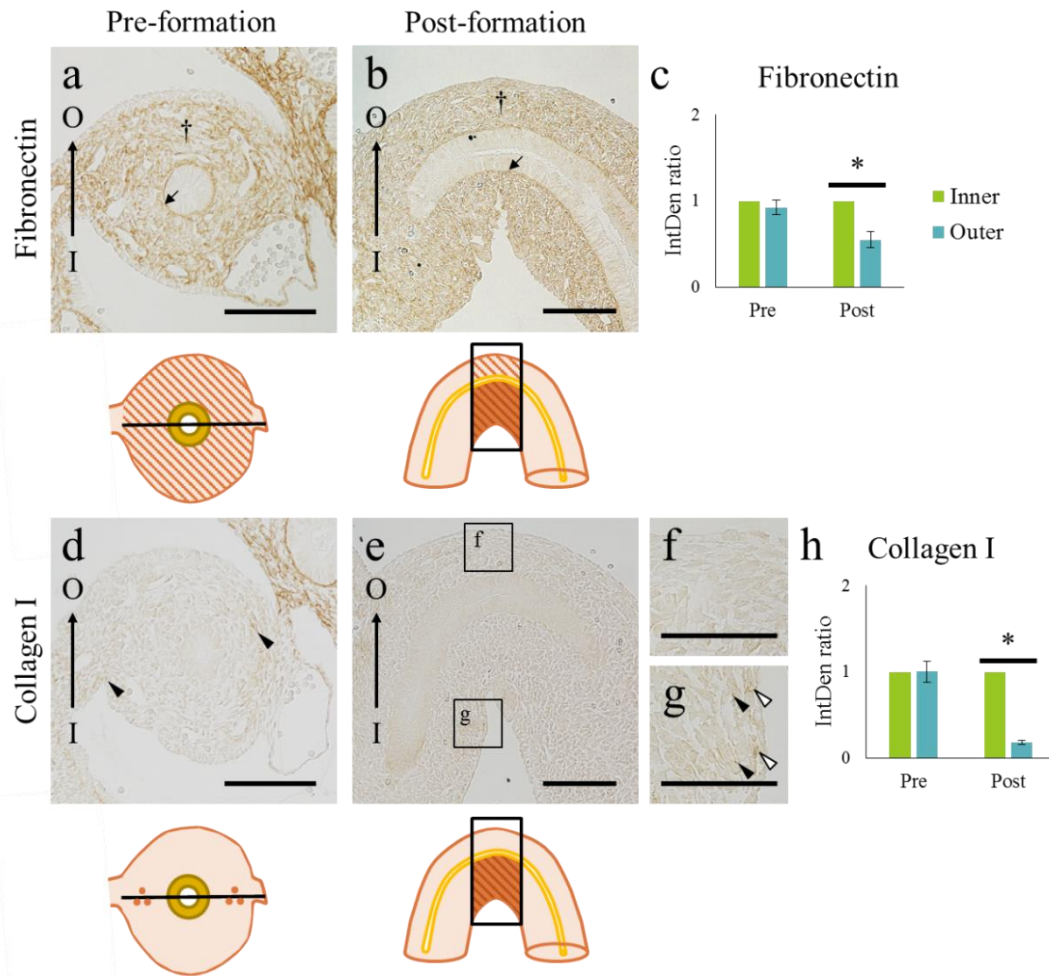


Figure 3-7. Distribution of fibronectin and collagen I in the mesenchymal area of the developing mouse duodenojejunal flexure (DJF).

(a and b) Immunohistochemistry for fibronectin at the pre-formation (a) and post-formation (b) stage DJFs. Arrows, immunopositive basement membranes; bars, 100 μ m; †, immunopositive intercellular space.

(c) Comparison of the integrated density (IntDen) ratio for fibronectin-positivity.

(d–g) Immunohistochemistry for collagen I at the pre-formation (d) and post-formation (e) stage DJFs. (f and g) are high magnification views in the inner (g) and outer (f) sides of (e). Bars, 100 μ m (d and e) and 50 μ m (f and g); black arrowheads, scattered immunopositivity; I, inner side; O, outer side; white arrowheads, assembled immunopositivity. Schemas beneath the pictures summarize the IntDen ratio difference. Darker brown indicates higher IntDen ratio.

(h) Comparison of the IntDen ratio for collagen I-positivity. Values = mean \pm standard error; $n \geq 4$; *, significant difference between the inner and outer side (Wilcoxon test, $P < 0.05$).

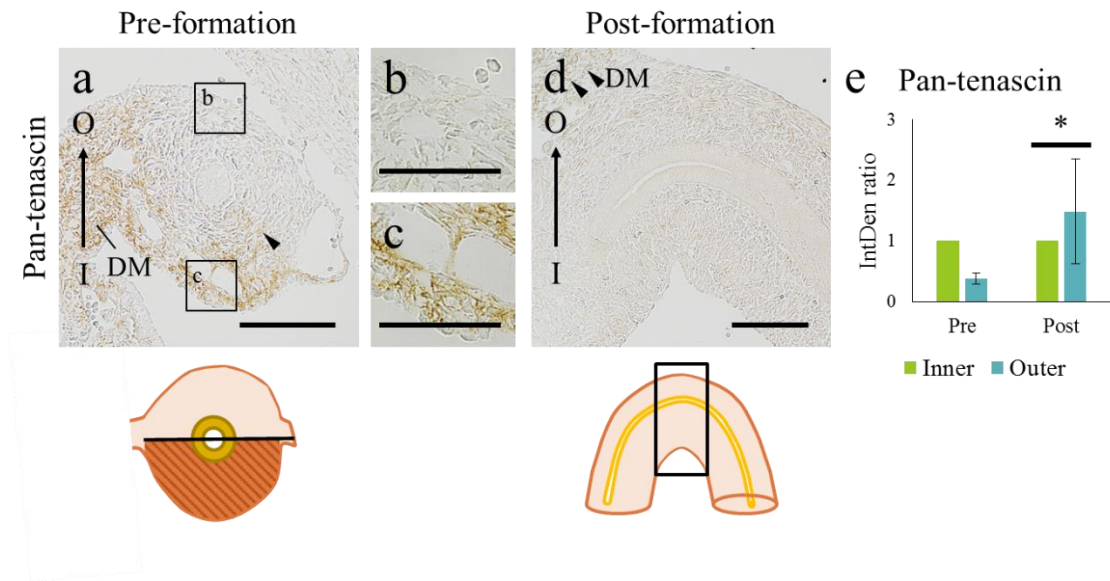


Figure3-8. Distribution of pan-tenascin in the mesenchymal area of the developing mouse duodenojejunal flexure (DJF).

(a–d) Immunohistochemistry for pan-tenascin at the pre-formation (a) and post-formation (d) stage DJF. (b and c) are high magnification views in the inner (c) and outer (b) sides of (a). Arrowheads, immunopositive intercellular space; bars, 100 μ m (a and d) and 50 μ m (b and c); DM, dorsal mesentery; I, inner side; O, outer side.

(e) Comparison of the integrated density (IntDen) ratio for the pan-tenascin-positivity. Values = mean \pm standard error; $n \geq 4$; *, significant difference between the inner and outer side (Wilcoxon test, $P < 0.05$).

Schemas beneath the pictures summarize the IntDen ratio difference. Darker brown indicates higher IntDen ratio.

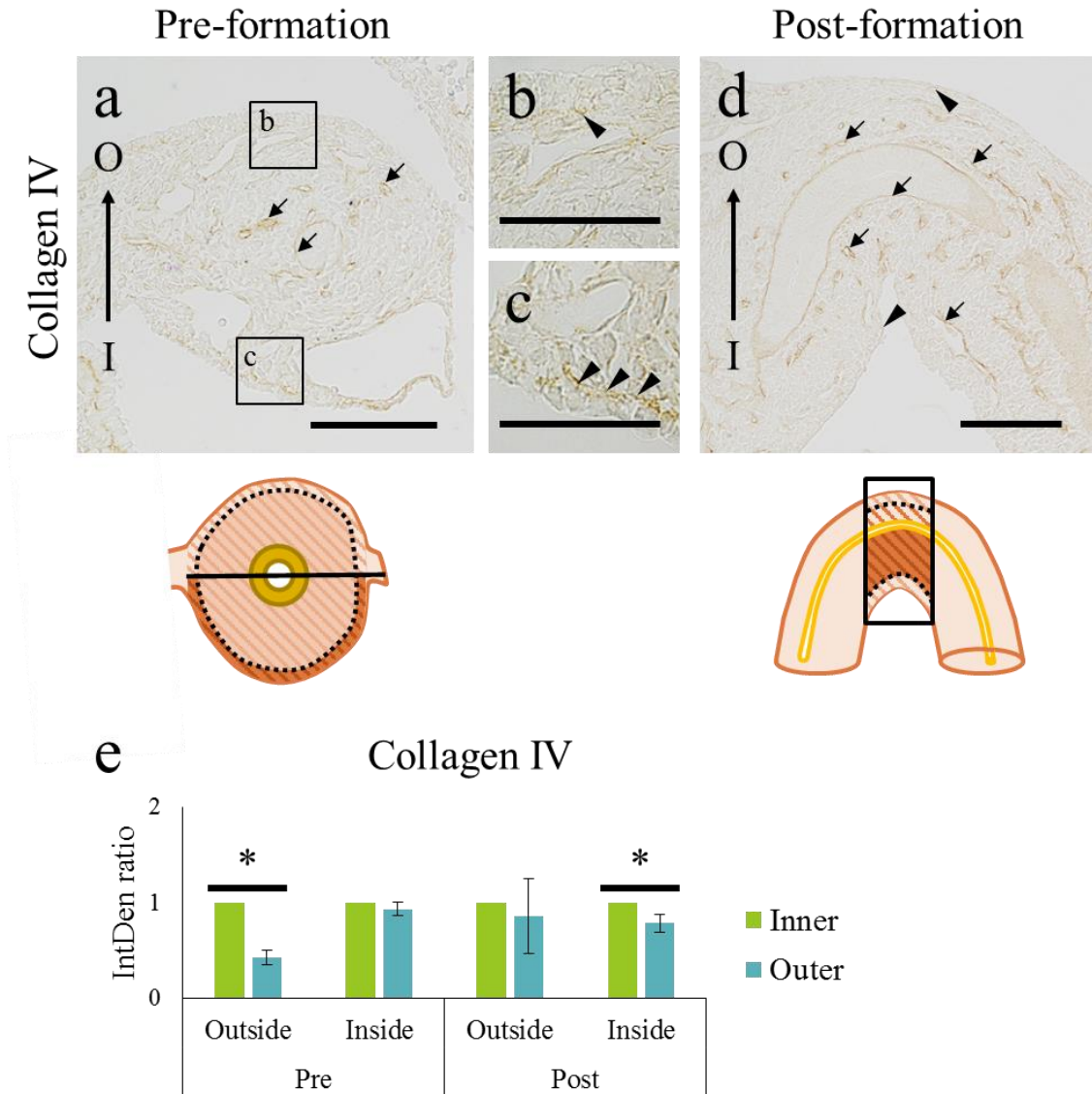


Figure 3-9. Distribution of collagen IV in the mesenchymal area of the developing mouse duodenojejunal flexure (DJF).

(a–d) Immunohistochemistry for collagen IV at the pre-formation (a) and post-formation (d) stage DJFs. (b and c) are high magnification views in the inner (c) and outer (b) sides of (a). Arrows, immune-positive mucosal epithelial and endothelial basement membranes; arrowheads, immunopositive mesothelial basement membrane; bars, 100 μm (a and d) and 50 μm (b and c); I, inner side; O, outer side.

(e) Comparison of the integrated density (IntDen) ratio for the collagen IV-positivity. Values = mean \pm standard error; $n \geq 4$; *, significant difference between the inner and outer side (Wilcoxon test, $P < 0.05$).

Schemas beneath the pictures summarize the IntDen ratio difference. Darker brown indicates higher IntDen ratio.

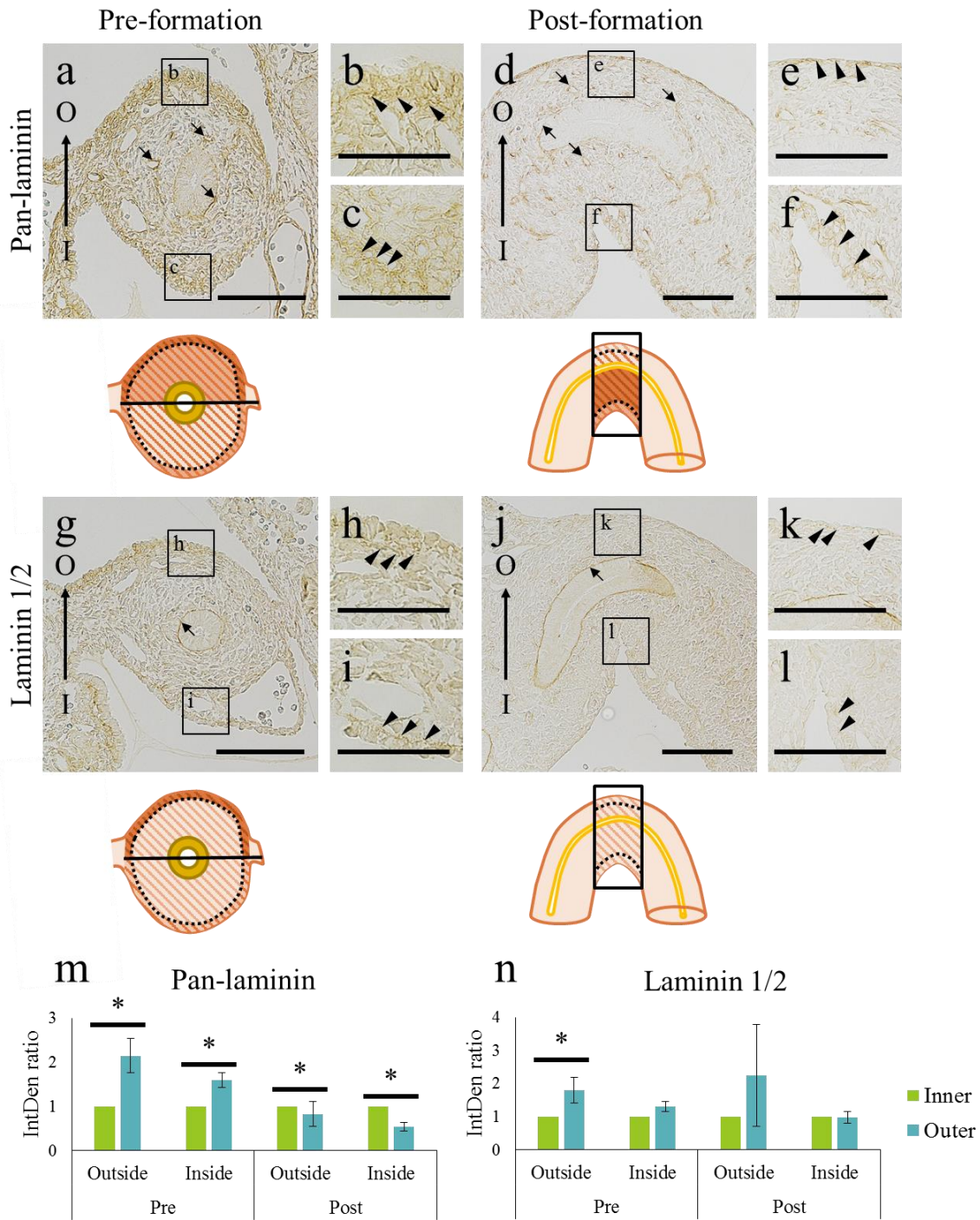


Figure 3-10. Distribution of pan-laminin- and laminin 1/2 in the mesenchymal area of the developing mouse duodenojejunal flexure (DJF).

(a–f) Immunohistochemistry for pan-laminin at the pre-formation (a) and post-formation (d) stage DJFs. (b and c) are high magnification views in the inner (c) and outer (b) sides of (a), and (e and f) are high magnification views in the inner (f) and outer (e) sides of (d).

(g–l) Immunohistochemistry for laminin 1/2 at the pre-formation (g) and post-formation (j) stage DJFs. (h and i) are high magnification views in the inner (i) and outer (h) sides of (g), and (k and l) are high magnification views in the inner (l) and outer (k) sides of (j). Arrows, immunopositive mucosal epithelial and endothelial basement membranes; arrowheads, immunopositive mesothelial basement membrane; bars, 100 μm (g and j) and 50 μm (h, i, k and l).

(m and n) Comparison of the integrated density (IntDen) ratio for the pan-laminin- (m) and laminin 1/2-positivity (n). Values = mean \pm standard error; $n \geq 4$; *, significant difference between the inner and outer side (Wilcoxon test, $P < 0.05$).

Schemas beneath the pictures summarize the IntDen ratio difference. Darker brown indicates higher IntDen ratio.

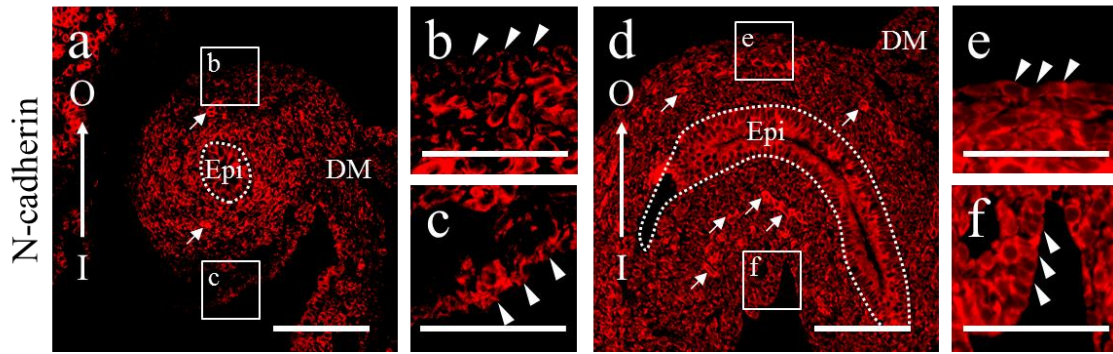


Figure 3-11. Distribution of N-cadherin in the mesothelium of the developing mouse duodenojejunal flexure (DJF).

(a–f) Immunohistochemistry for N-cadherin at the pre-formation (a) and post-formation (d) stage DJFs. (b and c) are high magnification views in the inner (c) and outer (b) sides of (a), and (e and f) are high magnification views in the inner (f) and outer (e) of (d). Arrows, immunopositive neural crest cells and neurons; arrowheads, immunopositive mesothelial cells; bars, 100 μm (a and d) and 50 μm (b, c, e and f); DM, dorsal mesentery; Epi, mucosal epithelium; I, inner side; O, outer side.

Table 3-3. Summary of the analyses of the gut component cells and extracellular matrix (ECM) molecules

Gut component	Pre-formation*	Post-formation*	ECM	Pre-formation*	Post-formation*
Mucosal epithelium	—	—	pH1.0 AB	—	Inner > Outer
Pan-mesenchyme	—	Inner > Outer	pH2.5 AB	Inner < Outer	Inner > Outer
Smooth muscle	Not detected	Not detected	Fibronectin	—	Inner > Outer
Lymphatic endothelium	Not detected	Not detected	Collagen I	—	Inner > Outer
Vascular endothelium	—	Inner > Outer (CD31)	Pan-tenascin	Inner > Outer	—
Neural crest	—	—	Collagen IV	Inner > Outer at outside	Inner > Outer at inside
Neuron	Inner > Outer at outside	Inner > Outer at outside	Pan-laminin	Inner < Outer	Inner > Outer
			Laminin 1/2	Inner < Outer at outside	—

* < and > indicate the side with a higher value between the inner and outer bending sides of the duodenojejunal flexure. AB, Alcian Blue.

Conclusion

The gut morphology effects on the digestive function and is related to feeding habit of each species. In addition, the deformity including intestinal malrotation is reported in both human and animal, and it may develop to intestinal volvulus and acute emergency. Therefore, elucidating gut morphogenesis is needed to understand gut physiology and pathology.

In mice, gut morphogenesis starts as pits which will give rise to the cranial intestinal portal and the caudal intestinal portal, at around embryonic day (E) 7.0. Between E9.0 and E9.5, the endoderm surrounded by mesenchyme finishes folding and exists as a closed gut tube which consists of foregut, midgut, and hindgut. Simultaneously, the midgut begins to make a primary loop and grows into the umbilical cord as physiological umbilical herniation at around E10.5. This herniation continues until around E16.0. During primary gut loop formation to physiological herniation, the gut tube experiences rotation, elongation, and flexure formation. In particular, flexure formation is important for the compaction of the gut tube which is extremely longer than the body length to fit into the abdominal cavity. Those flexures are organized not to disturb the digestion system. In the jejunum and ileum, it has been reported that the interaction between the gut tube and its dorsal mesentery is important to form complex flexures. However, the mechanism under gut flexure formation has not been investigated enough. The aim of this study is to elucidate the mechanisms of gut flexure formation through morphological approach.

In Chapter 1, the author investigated the gut morphologies in prenatal and postnatal

mice to explore the suitable part of the gut tube for the analysis of flexure formation. In the postnatal mice, the gut morphology differed among individuals at the jejunum and ileum, not although it was almost the same at the duodenum including the duodenojejunal flexure (DJF) and colon. Since most parts of the jejunum and ileum are loosely fixed with the mesentery to the abdominal wall, those parts seemed to be affected by the peristalsis covering the regular flexures conserved among individuals by irregular flexures. On the other hand, in prenatal mice, the gut morphology was almost the same among individuals at the same embryonic days from E10.75 to E13.75. The gut flexures were observed in the two parts: the part in the abdominal cavity behind the stomach and the part out of the abdominal cavity as physiological umbilical herniation. In the herniation, flexures overlapped each other, making it difficult to distinguish each flexure. However, the flexure in the abdominal cavity considered as the DJF was independently and clearly observed apart from other flexures. Therefore, the author investigated mouse DJF formation as a flexure formation model in detail. DJF formation occurred from E10.75 to E11.75, and the tip of the DJF faced to the dorsal direction along the body axis. From E12.75, the two legs of the DJF elongated toward the left cranial direction along the body axis, surrounding the caudal part of the stomach. According to the observation of the attaching portion of the mesentery, the author clarified that DJF formation along the dorsal-ventral body axis turned out to be along the left-right intestinal axis due to the counterclockwise rotation around the cranial-caudal intestinal axis. Recent studies showed that the asymmetric elongation rate between the gut and its dorsal mesentery was involved with flexure formation in the herniation. However, the process of DJF formation

seemed to be different from that of flexure formation in the herniation. Therefore, these results suggest that the mouse DJF is a useful model to investigate a novel mechanism of flexure formation. The author investigated mouse DJF formation in the following research.

In Chapter 2, the author investigated histological features of mouse DJF formation at the pre-formation stage (E10.75) and the post-formation stage (E11.25–E11.75). The DJF showed several asymmetric morphologies between the inner and outer bending sides as followings. The cell morphologies in the mesothelial area were significantly different between the both sides in the DJF at the pre-formation and post-formation stages. The DJF at the post-formation stage had thicker gut wall in the inner side and more proliferation rate in the outer side than the opposite sides. In the transmission electron microscope observation at the post-formation stage, the mesenchymal cells in the inner side elongated along the inner-outer bending axis and connected each other via a few long adherens junctions with narrow intercellular spaces, while those in the outer side elongated along perpendicular to the bending axis and connected each other by cytoplasmic processes via abundant short adherens junctions with large intercellular spaces. These asymmetric morphologies suggest the establishment of the asymmetric elongation rate between the inner and outer bending sides of the DJF along the cranial-caudal intestinal axis. Therefore, the author assumes that the direct power to form mouse DJF bending is the asymmetric morphologies between the inner and outer bending sides.

In Chapter 3, the author investigated the distributions of the gut component cells and extracellular matrix (ECM) molecules in the mouse DJF as the candidate factors to

establish the asymmetric morphologies. For the distributions of the gut component cells, the distributions of the pan-mesenchymal cells and blood vessels that were major components of the mesenchymal area showed higher in the inner side than in the outer side of the post-formation stage DJF, representing the high cell density in the inner side observed in Chapter 2. The number of the positive cells for Tuj1, a neural marker, was also more abundant in the inner side than in the outer side of the DJF at both stages, while that of the positive cells for Sox10, a immature neuron marker, was not different between the two sides. Therefore, the author assumes that neural differentiation occurs earlier in the inner side than in the outer side during DJF formation. For the distributions of the ECM molecules, the author investigated the following molecules related to organ morphogenesis: proteoglycans, pan-tenascin, fibronectin, collagen I, collagen IV, pan-laminin, and laminin 1/2. The distribution analysis revealed that all molecules showed the asymmetric distributions between the inner and outer bending sides of the DJF and that the patterns of those distributions changed during DJF formation. In particular, the basement membrane ECM, collagen IV, and laminins, showed its asymmetric distribution at the mesothelial area of the pre-formation stage DJF, and the N-cadherin-positivity at that area was also different between the inner and outer bending sides of the pre-formation stage DJF. Those results of the distribution of the gut component cells and ECM molecules suggest their involvement with the establishment of the asymmetric morphologies during DJF formation.

In conclusion, the author indicates that the mouse DJF is a useful flexure formation model controlled under the mechanism different from that in flexure formation in the

herniation that needs the interaction with the dorsal mesentery. In mouse DJF formation, the gut original asymmetric morphologies between the inner and outer bending sides are important to make the asymmetric elongation between the two sides to complete DJF bending. The DJF is an important part for gut rotation, and its morphological change is similar with that of the species-specific ascending colon. Therefore, this study gives good understandings for gut embryology in both human and animal. In addition, the author strongly believes that the finding of this novel mechanism of flexure formation is useful in the field of not only gut morphogenesis, but also other organogenesis.

References

1. Adams, SD. and Stanton, MP. 2014. Malrotation and intestinal atresias. *Early Hum. Dev.*, **90**: 921–925.
2. Akbareian, SE., Nagy, N., Steiger, CE., Mably, JD., Miller, SA., Hotta, R., Molnar, D. and Goldstein, AM. 2013. Enteric neural crest-derived cells promote their migration by modifying their microenvironment through tenascin-C production. *Dev. Biol.*, **382**: 446–456.
3. Bondow, BJ., Faber, ML., Wojta, KJ., Walker, EM. and Battle, MA. 2012. E-cadherin is required for intestinal morphogenesis in the mouse. *Dev. Biol.*, **371**: 1–12.
4. Breau, MA., Dahmani, A., Broders-Bondon, F., Thiery, JP. and Dufour, S. 2009. β 1 integrins are required for the invasion of the caecum and proximal hindgut by enteric neural crest cells. *Development*, **136**: 2791–2801.
5. Burn, SF. and Hill, RE. 2009. Left-right asymmetry in gut development: what happens next? *Bioessays*, **31**: 1026–1037.
6. Chiquet-Ehrismann, R. and Tucker, RP. 2011. Tenascins and the importance of adhesion modulation. *Cold Spring Harb. Perspect. Biol.*, **3**: a004960
7. Davis, NM., Kurpios, NA., Sun, X., Gros, J., Martin, JF. and Tabin, CJ. 2008. The chirality of gut rotation derives from left-right asymmetric changes in the architecture of the dorsal mesentery. *Dev. Cell*, **15**: 134–145.
8. De Arcangelis, A., Neuville, P., Boukamel, R., Lefebvre, O., Kedinger, M. and Simon-Assmann, P. 1996. Inhibition of Laminin α 1-chain expression leads to alteration of basement membrane assembly and cell differentiation. *J. Cell Biol.*, **133**: 417–430.
9. Dyce, KM., Sack, WO. and Wensing, CJGW. 1998. Textbook of veterinary anatomy, second edition, Japanese translation. pp. 117–122. Kindai Shyppan,

Tokyo, Japan.

10. Faure, S., McKey, J., Sagnol, S. and de Santa Barbara, P. 2015. Enteric neural crest cells regulate vertebrate stomach patterning and differentiation. *Development*, **142**: 331–342.
11. Gelse, K., Pöschl, E. and Aigner, T. 2003. Collagens—structure, function, and biosynthesis. *Adv. Drug Deliv. Rev.*, **55**: 1531–1546.
12. Geiger, B., Spatz, JP. and Bershadsky, AD. 2009. Environmental sensing through focal adhesions. *Nat. Rev. Mol. Cell Biol.*, **10**: 21–33.
13. Grainger, S., Savory, JG. and Lohnes, D. 2010. Cdx2 regulates patterning of the intestinal epithelium. *Dev. Biol.*, **339**: 155–165.
14. Harrison, C. and Shepherd, IT. 2013. Choices choices: regulation of precursor differentiation during enteric nervous system development. *Neurogastroenterol. Motil.*, **25**: 554–562.
15. Hohenester, E. and Yurchenco, PD. 2013. Laminins in basement membrane assembly. *Cell Adh. Migr.*, **7**: 56–63.
16. Hynes, RO. 2009. The extracellular matrix: not just pretty fibrils. *Science*, **326**: 1216–1219.
17. Iozzo, RV. and Schaefer, L. 2015. Proteoglycan form and function: A comprehensive nomenclature of proteoglycans. *Matrix Biol.*, **42**: 11–55.
18. Janoštiak, R., Pataki, AC., Brábek, J. and Rösel, D. 2014. Mechanosensors in integrin signaling: the emerging role of p130Cas. *Eur. J. Cell Biol.*, **93**: 445–454.
19. Jones, C. and Chen P. 2007. Planer cell polarity signaling in vertebrates. *BioEssays*, **29**: 120–132.
20. Jones, FS. and Jones, PL. 2000. The tenascin family of ECM glycoproteins: structure, function, and regulation during embryonic development and tissue

- remodeling. *Dev. Dyn.*, **218**: 235–259.
21. Khoshnoodi, K., Pedchenko, V. and Hudson, BG. 2008. Mammalian Collagen IV. *Microsc. Res. Tech.*, **71**: 357–370.
 22. Kim, KE., Sung, H. and Koh, GY. 2007. Lymphatic development in mouse small intestine. *Dev. Dyn.*, **236**: 2020–2025.
 23. Kim, SH., Turnbull, J. and Guimond, S. 2011. Extracellular matrix and cell signaling: the dynamic cooperation of integrin, proteoglycan and growth factor receptor. *J. Endocrinol.*, **209**: 139–151.
 24. Kluth, D., Jaeschke-Melli, S. and Fiegel, H. 2003. The embryology of gut rotation. *Semin. Pediatr. Surg.*, **12**: 275–279.
 25. König, HE. and Liebich, HG. 2007. Veterinary anatomy of domestic mammals, Textbook and colour atlas, 3rd edition, Japanese translation. pp. 373–386. Midori-Shobo, Tokyo, Japan.
 26. Kurpios, NA., Ibañes, M., Davis, NM., Lui, W., Katz, T., Martin, JF., Izpisua Belmonte, JC. and Tabin, CJ. 2008. The direction of gut looping is established by changes in the extracellular matrix and in cell: cell adhesion. *Proc. Natl. Acad. Sci. U S A.*, **105**: 8499–8506.
 27. Labat-Robert, J. 2012. Cell-Matrix interactions, the role of fibronectin and integrins. A survey. *Pathol. Biol.*, **60**: 15–19.
 28. Lake, JI. and Heuckeroth, RO. 2013. Enteric nervous system development: migration, differentiation, and disease. *Am. J. Physiol. Gastrointest. Liver Physiol.*, **305**: G1–G24.
 29. Legate, KR., Wickström, SA. and Fässler, R. 2009. Genetic and cell biological analysis of integrin outside-in signaling. *Genes Dev.*, **23**: 397–418.
 30. Leitinger, B. 2011. Transmembrane collagen receptors. *Annu. Rev. Cell Dev. Biol.*, **27**: 265–290.

31. Levin, M. 2005. Left-right asymmetry in embryonic development: a comprehensive review. *Mec. Dev.*, **122**: 3–25.
32. Linask, KK., Han, M., Cai, DH., Brauer, PR. and Maisastry, SM. 2005. Cardiac morphogenesis: matrix metalloproteinase coordination of cellular mechanisms underlying heart tube formation and directionality of looping. *Dev. Dyn.*, **233**: 739–753.
33. Liu, JA. and Ngan, ES. 2014. Hedgehog and notch signaling in enteric nervous system development. *Neurosignals*, **22**: 1–13.
34. Mao, J., Kim, BM., Rajurkar, M., Shivdasani, RA. and McMahon, AP. 2010. Hedgehog signaling controls mesenchymal growth in the developing mammalian digestive tract. *Development*, **137**: 1721–1729.
35. Muller, JK., Prather, DR. and Nascone-Yoder, NM. 2003. Left-right asymmetric morphogenesis in the *Xenopus* digestive system. *Dev. Dyn.*, **228**: 672–682.
36. Nehra, D. and Goldstein, AM. 2011. Intestinal malrotation: varied clinical presentation from infancy through adulthood. *Surgery*, **149**: 386–393.
37. Nekrep, N., Wang, J., Miyatsuka, T. and German, MS. 2008. Signals from the neural crest regulate beta-cell mass in the pancreas. *Development*, **135**: 2151–2160.
38. Noah, TK., Donahue, B. and Shroyer, NF. 2011. Intestinal development and differentiation. *Exp. Cell Res.*, **317**: 2702–2710.
39. Noden, DM. and Lahunta, AD. 1991. The embryology of domestic animals, Developmental mechanisms and malformations, Japanese translation. pp. 298–305. Gakusosha, Tokyo, Japan.
40. Plageman, TF., Jr., Zacharias, AL., Gage, PJ. and Lang, RA. 2011. Shroom3 and a Pitx2-N-cadherin pathway function cooperatively to generate asymmetric cell shape changes during gut morphogenesis. *Dev. Biol.*, **357**: 227–234.

41. Plotnikov, SV., Pasapera, AM., Sabass, B. and Waterman, CM. 2012. Force fluctuations within focal adhesions mediate ECM-rigidity sensing to guide directed cell migration. *Cell*, **151**: 1513–1527.
42. Pöschl, E., Schlötzer-Schrehardt, U., Brachvogel, B., Saito, K., Ninomiya, Y. and Mayer, U. 2003. Collagen IV is essential for basement membrane stability but dispensable for initiation of its assembly during early development. *Development*, **131**: 1619–1628.
43. Powell, DW., Pinchuk, IV., Saada, JI., Chen, X. and Mifflin, RC. 2011. Mesenchymal cells of the intestinal lamina propria. *Annu. Rev. Physiol.*, **73**: 213–237.
44. Reed, RA., Womble, MA., Dush, MK., Tull, RR., Bloom, SK., Morckel, AR., Devlin, EW. and Nascone-Yoder, NM. 2009. Morphogenesis of the primitive gut tube is generated by Rho/ROCK/myosin II-mediated endoderm rearrangements. *Dev. Dyn.*, **238**: 3111–3125.
45. Savin, T., Kurpios, NA., Shyer, AE., Florescu, P., Liang, H., Mahadevan, L. and Tabin, CJ. 2011. On the growth and form of the gut. *Nature*, **476**: 57-62.
46. Shyer, AE., Tallinen, T., Nerurkar, NL., Wei, Z., Gil, ES., Kaplan, DL., Tabin, CJ. and Mahadevan, L. 2013. Villification: how the gut gets its villi. *Science*, **342**: 212–218.
47. Shimokawa, K., Kimura-Yoshida, C., Nagai, N., Mukai, K., Matsubara, K., Watanabe, H., Matsuda, Y., Mochida, K. and Matsuo, I. 2011. Cell surface heparan sulfate chains regulate local reception of FGF signaling in the mouse embryo. *Dev. Cell*, **21**: 252–272.
48. Shiraishi, I., Takamatsu, T., Minamikawa, T. and Fujita, S. 1992. 3-D observation of actin filaments during cardiac myofibriogenesis in chick embryo using a confocal laser scanning microscope. *Anat. Embryol. Berl.*, **185**: 401–

- 408.
49. Sidney, LE., Branch, MJ., Dunphy, SE., Dua, HS. and Hopkinson, A. 2014. Concise review: evidence for CD34 as a common marker for diverse progenitors. *Stem Cells*, **32**: 1380–1389.
 50. Simon-Assmann, P., Lefebvre, O., Bellissent-Waydelich, A., Olsen, J., Orian-Rousseau, V. and Dearcangelis, A. 1998. The Laminins: role in intestinal morphogenesis and differentiation. *Ann. N. Y. Acad. Sci.*, **859**: 46–64.
 51. Soufan, AT., van den Berg, G., Ruijter, JM., de Boer, PA., van den Hoff, MJ. and Moorman, AF. 2006. Regionalized sequence of myocardial cell growth and proliferation characterizes early chamber formation. *Circ. Res.*, **99**: 545–552.
 52. Spence, JR., Lauf, R. and Shroyer, NF. 2011. Vertebrate intestinal endoderm development. *Dev. Dyn.*, **240**: 501–520.
 53. Tondeleir, D., Vandamme, D., Vandekerckhove, J., Ampe, C. and Lambrechts, A. 2009. Actin isoform expression patterns during mammalian development and in pathology: insights from mouse models. *Cell Motil. Cytoskeleton*, **66**: 798–815.
 54. Wallingford, JB., Fraser, SE. and Harland, RM. 2002. Convergent extension: The molecular control of polarized cell movement during embryonic development. *Dev. Cell*, **2**: 695–706.
 55. Welsh, IC., Thomsen, M., Gludish, DW., Alfonso-Parra, C., Bai, Y., Martin, JF. and Kurpios, NA. 2013. Integration of left-right Pitx2 Transcription and Wnt signaling drives asymmetric gut morphogenesis via Daam2. *Dev. Cell*, **26**: 629–644.
 56. Whiting, CV., Tarlton, JF., Bailey, M., Morgan, CL. and Bland, PW. 2003. Abnormal mucosal extracellular matrix deposition is associated with increased TGF-beta receptor-expressing mesenchymal cells in a mouse model of colitis.

J. Histochem. Cytochem., **51**: 1177–1189.

57. Yamada, M., Udagawa, J., Matsumoto, A., Hashimoto, R., Hatta, T., Nishita, M., Minami, Y. and Otani, H. 2010. Ror2 is required for midgut elongation during mouse development. *Dev. Dyn.*, **239**: 941–953.

Acknowledgements

First and foremost, I would like to express my gratitude towards my supervisor Dr. Yasuhiro Kon for his support, advice, and guidance throughout the duration of this project. I would like to thank Dr. Osamu Ichii, Dr. Mitsuyoshi Takiguchi, and Dr. Kentaro Sakamoto for time taken to provide their advice, critical comments and assistance in completing this thesis. I would also like to thank Dr. Saori Kanazawa, and all the members of the laboratory of anatomy for their encouragement, support, advice, and great times. Finally, I deeply appreciated to the animals supporting this study.

Conclusion in Japanese

腸管の形態形成機序の解析

— マウス十二指腸空腸曲形成にみられる時空間的制御 —

北海道大学大学院獣医学研究科

比較形態機能学講座 解剖学教室

尾之内 佐和

腸管形態は消化機能に影響し、様々な動物種においてその食性を反映する。また、腸管奇形、特に腸管回転異常はヒト及び動物で観察され、時に激しい急性症状を引き起こし、外科的な治療が必要となる。よって、腸管形態形成に関する研究は腸管生理や腸管奇形の病理を理解するうえで重要な基礎的知識をもたらす。

マウスにおいて、腸管は頭側羊膜ヒダ直下の内胚葉に存在する小さな溝(前腸ポケット)として胎齢7日頃より発生し、胎齢9日には前腸、中腸及び後腸からなる1本の連続した管となる。さらに胎齢10.5日頃には中腸に臍ループを形成し始め、生理的臍ヘルニアとして体外へ突出し、胎齢16日まで持続する。この原始腸管形成から臍ヘルニア終了までの間に腸管の伸長、回転、屈曲形成が行われる。腸管屈曲は腸管を腹腔内へ収納するために必要であり、この屈曲は消化機能を阻害しないよう規則的に配置する。また、腸管屈曲は種特異的又は種間共通の腸管形態を特徴づける。本研究では、形態学的アプローチから屈曲形成の機序を解明することを目的とした。

第一章ではマウスの腸管形態を胎子から生後個体で肉眼的に観察し、屈曲形成の観察に適した部位を検討した。生後個体の腸管は十二指腸および結腸を除き、空回腸の多くの部位の走行が個体間で異なった。十二指腸および結腸は腸間膜により腹腔壁にしっかりと固定されているが、空回腸ではその固定が緩いため、空回腸で特に蠕動運動の影響を強く受け、蠕動運動による偶発的な屈曲が観察されたと考えられる。一方、胎子の腸管の走行は、同胎齢の個体で走行が一致した。腸管の屈曲は観察期間において二か所に見られ、腹腔内で胃の直後に観察されるものと生理的臍ヘルニアとして腹腔外で観察されるものがあった。生理的臍ヘルニアの部分は複数の屈曲が組み合わされた複雑な構造となっており、1つ1つの屈曲を明確に区別することが困難であった。一方、腹腔内の胃の直後に観察される十二指腸空腸曲は胎子から生後個体まですべての個体で容易に観察され、その形成が他の屈曲と独立して起こることから、屈曲形成モデルとして以降の観察に用いることにした。十二指腸空腸曲は胎齢 10.75 日から胎齢 11.75 日の間に体軸の背側へその頂点を向けた屈曲を形成する。胎齢 12.75 日以降は屈曲を形成する二本の脚が伸長し、体軸の左前方へ屈曲の頂点を向けて胃を後ろから囲むような形態が観察された。提出者は背側腸間膜の付着位置の観察から、十二指腸空腸曲の屈曲過程における回転により、体軸背-腹方向に観察される十二指腸空腸曲の屈曲が、実質的には腸管軸左-右方向の屈曲であることを見出した。特に近年、臍ヘルニアにおける屈曲形成は腸間膜と腸管の伸長率の差によって物理的に起こることが提唱されている。しかしながら、前述の十二指腸空腸曲の形成過程は臍ヘルニアで観察される複数の屈曲の形成とは異なる形態を示すため、十二指腸空腸曲形成には腸間膜との相互作用とは別の新たな屈曲形

成機序の存在が示唆された。

第二章ではマウス十二指腸空腸曲の組織切片を観察し、形態学的特徴を観察した。観察は屈曲形成前(胎齢 10.75 日)及び屈曲形成後(胎齢 11.25 日から 11.75 日)に分けて行った。十二指腸空腸曲の組織像は屈曲内側と屈曲外側で非対称的な特徴を示し、腸壁の厚さが屈曲内側で大きい一方、細胞増殖は屈曲外側が高くなった。また、腸壁の最外層を構成する細胞(中皮細胞)の形態が屈曲内-外側で異なった。屈曲形成後の透過型電子顕微鏡観察では、腸管壁構成細胞の形態が、屈曲内側で屈曲軸方向に長く、少数であるが幅の広い細胞接着装置により密に分布する像が観察された。一方、屈曲外側では腸管壁構成細胞が細胞突起を伸ばし、多数の短い細胞接着装置により屈曲内側と比べて疎に分布する像が観察された。これらの観察された形態差はいずれも腸管の吻-尾側方向において屈曲内-外側の伸長差を形成することを示唆する。以上から、十二指腸空腸曲の屈曲の直接的な原動力は屈曲内-外側で観察される非対称的形態であると考えられた。

第三章では十二指腸空腸曲を構成する細胞成分及び細胞外基質を観察し、屈曲内-外側で比較した。細胞成分では、腸管壁の主たる成分である間葉細胞と血管内皮細胞の分布が屈曲形成後に屈曲内側で外側よりも高くなった。これは、第二章で観察された屈曲形成後の屈曲内側の細胞が密に分布することを反映するものと考えられた。また、神経細胞マーカー(Tuj1)陽性細胞が、屈曲形成前及び形成後のいずれも、腸管壁において屈曲内側で外側より有意に多く、細胞体も大きい傾向にあった。その一方で、十二指腸空腸曲に分布する未分化神経細胞マーカー(Sox10)の陽性反応に屈曲内-外側の差はないことから、十二指腸空腸曲

形成過程において、神経細胞の分化が屈曲内側で亢進すると考えられた。細胞外基質はプロテオグリカン及び Pan-tenascin、Fibronectin、Collagen I、Collagen IV、Pan-laminin、Laminin 1/2 について観察した。いずれも屈曲内-外側において特有の局在パターンと変遷が観察された。特に基底膜を構成する細胞外基質 (Collagen IV、Pan-laminin、Laminin 1/2) は中皮細胞領域の基底膜に屈曲内-外側の差が観察され、この部位の細胞接着を N-cadherin の免疫染色で観察すると、屈曲形成前の屈曲内-外側でその様相が異なった。観察した細胞外基質はいずれも形態形成に関する作用が報告されている。以上の結果から、これらの屈曲内-外側で非対称的な分布を示す細胞・細胞外基質がマウス十二指腸空腸曲の形態変化を誘導すると考察された。

結論として、マウス十二指腸空腸曲に見られる屈曲形成機序は臍ヘルニア部で見られるような腸間膜とのかかわりによるものとは別の、腸管そのものが持つ屈曲内-外側の形態差によって起こると考えられる。十二指腸空腸曲は発生過程において腸管の回転にも関与することが示唆されており、また、その形成過程は動物種差を示す上行結腸の形態変化と類似する。よって、本研究は腸管発生研究に重要な知見を提供する。また、この新たな屈曲形成機序の発見は腸管形態形成だけでなく、他の臓器の形態形成機序の解明に重要な基礎的知見を与える。